

Experimental Characterization of Cryogenic Materials Contact Resistance

By

Kacie Salmon

A thesis submitted in partial fulfillment of the requirements for the degree of:

Master of Science

(Mechanical Engineering)

at the

UNIVERSITY OF WISCONSIN-MADISON

2021

Graduate Student: Kacie Salmon

Campus ID: 908-136-7857

Title: Experimental Characterization of Cryogenic Materials Contact Resistance

Approved by:

Professor Gregory Nellis

Department of Mechanical Engineering

Signature: _____ Date: _____

Professor John Pfothauer

Department of Mechanical Engineering

Signature: _____ Date: _____

Abstract

The thermal contact resistance associated with the interface made between high conductivity metals at cryogenic temperatures depends on several variables. Some of the primary factors include surface roughness, contact pressure, and the presence/type of thermal interface materials (TIMs). However, there are many secondary factors such as work-hardening, deformation, and pressure uniformity that lead to inherent non-repeatability in the thermal performance of pressed contacts. This variability limits the value of measurements for predicting the resistance of similar contacts or even the same contact reassembled. In this work, a test rig was designed and assembled for the precise measurement of thermal bulk and contact conductivity. This included fabrication of the test facility, assembly of instrumentation, the design and construction of a liquid helium dampening pot, and validation of the experimental setup. With the assembly of this test rig, experimental characterization of C101 and C110 bulk conductivity as well as a variety of contact measurements were carried out. Within our work, careful thermal contact resistance measurements for copper-copper interfaces under high pressure with and without TIMs were performed. In addition to these measurements, the measurement of the bulk conductivity of the same samples as well as detailed measurements of the surfaces and the uniformity of the contact pressure were documented. Finally, the work presents repeated measurements of the same sample made after mating and de-mating cycles. For these measurements presented here, we have provided an extremely detailed picture not only of the thermal contact resistance but also of the properties of the materials and surfaces associated with the joint.

Acknowledgements

There are many people who have made this work and my master's possible that I would like to thank. To my advisors Greg Nellis and John Pfothhauer, thank you for your continued support and mentorship throughout the last two years. I have grown tremendously as a researcher and an engineer within this program and could not have grown nearly as much without your guidance. I also cannot thank you both enough for the understanding and confidence that I was given working throughout this research. It isn't lost on me that it is a rare thing to be so happy with your relationship with your advisors and their guidance in your work.

I would also like to thank Kelsey McCusker at Northrop Grumman for her guidance and assistance throughout this research. Her experience and advice with the research as well as the equipment granted for our use were both invaluable to the success of this project. I would also like to thank Northrop Grumman for funding this research.

To my former undergraduate research assistants, Logan Kvalo and Kate Nelson, thank you for all your dedicated and enthusiastic work. I couldn't have asked for better students to help me and learn along the way. I'm sure you both will have bright futures ahead of you in any pursuits you desire.

And finally, to the SEL graduate students, thank you for all your help and friendship. In the many times I have been lost in my work, needed equipment, or just needed advice, they were always there and willing to help. It has been a special community to be a part of and I will miss it dearly. Thank you for making my master's program wonderful.

Table of Contents

Abstract.....	2
Acknowledgements.....	3
List of Figures.....	7
List of Tables	8
1 Introduction.....	9
1.1 Motivation.....	9
1.2 Contributions of Current Work.....	10
1.3 Thermal Contact Resistance/Conductance.....	11
2 Literature Review.....	14
2.1 Cryogenic Bulk Thermal Conductivity.....	14
2.2 Cryogenic Thermal Contact Resistance.....	16
2.2.1 Sources of Variability in Contact Resistance.....	21
2.3 Theoretical Models for Contact Resistance	21
2.3.1 Thermal Constriction Resistance	21
2.3.2 Boundary Resistance.....	23
2.3.3 Total Contact Resistance Model for Cryogenic Applications.....	24
3 Experimental Apparatus and Design.....	25
3.1 Vacuum Chamber and Cryocooler.....	25
3.2 Thermal Jackets and Sample Platform Design.....	26
3.2.1 Thermal Contraction Considerations	27
3.2.2 Sample Platform Design	28
3.3 Liquid Helium Dampening Pot and Revised Design	29
3.4 Bulk Conductivity Test Fixture.....	34

3.4.1 Temperature and Heat Flux Distribution	37
3.5 Contact Sample Holder Design.....	37
3.5.1 Fixture Thermal Resistance Measurement.....	40
3.6 Experimental Setup and Instrumentation	42
3.6.1 Instrumentation	42
3.6.2 Temperature Sensors and Heaters.....	43
4 Methodology and Calculations	45
4.1 Bulk Conductivity Measurement and Calculation	45
4.2 Contact Resistance	46
4.2.1 Surface Imaging and Pressure Application Measurement Methodology	49
4.3 Force Calculations for Contact Pressure Application	50
5 Results and Discussion	51
5.1 Uncertainty Analysis.....	51
5.1.1 Temperature Sensor Uncertainty	51
5.1.2 Applied Heat Uncertainty	53
5.1.3 Length and Cross-Sectional Area Measurement Uncertainty	55
5.1.4 Bulk Conductivity Total Uncertainty	56
5.1.5 Contact Resistance Total Uncertainty	57
5.2 Bulk Conductivity Results	58
5.2.1 Comparison with Literature and Expected RRR.....	60
5.3 Contact Resistance Results	60
5.3.1 Surface Imaging	63

5.3.2 Pressure Application	65
5.3.3 Comparison with Literature	67
6 Correlations and Theoretical Analysis	69
6.1 Constriction and Diffuse Mismatch Model.....	69
7 Conclusions and Future Work	71
References.....	73
Appendix A. Bulk Conductivity Test Procedure and Data Processing.....	76
Appendix B. Contact Resistance Test Procedure and Data Processing	85

List of Figures

Figure 1-1. Superconducting electrical resistivity and critical temperature [3].	9
Figure 1-2. Asperities and heat flow paths through a pressed contact [5].	12
Figure 1-3. Temperature distribution across materials and contact for a steady state heat flux [5].	13
Figure 2-1. Cryogenic thermal conductivity of copper [7].	14
Figure 2-2. NASA Cryogenic Thermal Conductivity Test Apparatus [6].	15
Figure 2-3. Van Sciver et al. experimental apparatus [8].	17
Figure 2-4. Contact sample holder in historical Northrop Grumman testing [10].	18
Figure 2-5. Salerno et. al contact conductance experimental apparatus [12].	20
Figure 3-1. Vacuum Chamber Exterior.	25
Figure 3-2. Cryocooler mounted within the vacuum chamber.	26
Figure 3-3. Thermal jackets mounted in bell jar on Sumitomo cryocooler.	26
Figure 3-4. Second stage copper sample plate.	28
Figure 3-5. Thermal jacket platform plates installed onto cryocooler.	29
Figure 3-6. Inherent thermal oscillations on testing platform on GM cryocooler.	30
Figure 3-7. Liquid helium dampening pot system.	31
Figure 3-8. Dampening system elements outside vacuum chamber.	32
Figure 3-9. Helium pot before and after thermal strap installation.	33
Figure 3-10. Dampened thermal oscillation results.	34
Figure 3-11. NGC T-beam design.	35
Figure 3-12. Current T-beam design with clamps.	36
Figure 3-13. Knife-edge clamps.	36
Figure 3-14. Second stage copper sample plate.	37
Figure 3-15. Contact resistance measurement test fixture.	38
Figure 3-16. Compressed contact fixture with interior view.	39
Figure 3-17. Fixture path measurement cradle and temperature sensor placement.	40

Figure 3-18. Fixture resistance measurements.....	41
Figure 3-19. Instrumentation setup schematic.	43
Figure 4-1. Contact fixture with temperature sensor placement.	47
Figure 4-2. Alicona surface imaging example.	49
Figure 5-1. Sequoia Brass & Copper C110 Bulk Conductivity Results	59
Figure 5-2. Sequoia Brass & Copper C101 Bulk Conductivity Results.	59
Figure 5-3. Comparison of C01 bulk conductivity with known RRR curves.	60
Figure 5-4. Dry contact Cu-Cu thermal resistance data.	61
Figure 5-5. Indium foil Cu-Cu contact thermal resistance data.	62
Figure 5-6. Apiezon-N grease Cu-Cu contact thermal resistance data.	63
Figure 5-7. Alicona G4 InfiniteFocus copper surface imaging.....	65
Figure 5-8. Pressure paper records for test matrix.	66
Figure 5-9. Comparison of dry Cu-Cu results with NGC data.	67
Figure 5-10. Comparison of indium Cu-Cu results with NGC data.	68
Figure 6-1. Theoretical comparison to S1R1 Dry.....	69
Figure 6-2. Theoretical comparison to S2R1 Dry.....	70

List of Tables

Table 3-1. Calculations for fixture resistance accounting.....	42
Table 3-2. Instrumentation for experimental setup.	42
Table 4-1. Nominal setpoints and corresponding minimum dT values.	46
Table 5-1. Test matrix.....	51
Table 5-2. Germanium sensor coefficients for uncertainty equations.	53
Table 5-3. Surface imaging results.	64

1 Introduction

1.1 Motivation

Superconducting electronics is an emerging technology that has many applications that might take advantage of the improvements in computer performance. Moore's Law, originated by the Intel cofounder Gordon Moore, predicted in the 1960s that due to the rapid improvement of computing technology, every two years the number of transistors on a microchip would double and effectively reduce the cost of computers by 50% [1]. While this held true for roughly fifty years, the trend is currently slowing, and exponential improvement is becoming increasingly more difficult to maintain. This is because current technology faces issues such as large energy consumption and dissipation within microchips as well as reaching the physical limitations in miniaturization of transistors [1].

As it becomes increasingly more difficult to increase the number of transistors on a microchip, superconducting electronics offer an alternative route to continue following the Moore's Law trend of increased performance. Superconductors are materials with a set of unique electrical and magnetic properties, including zero electrical resistance and ideal diamagnetism [2]. These properties occur in superconductors when they are below a certain critical temperature, prescribed by the material itself, as shown in Figure 1-1 for electrical resistance behavior. The zero electrical resistance in the superconducting wiring as well as the use of superconducting logic elements such as Josephson junction switches can greatly reduce the heat loss and increase the speed of processing, which both contribute to cost performance.

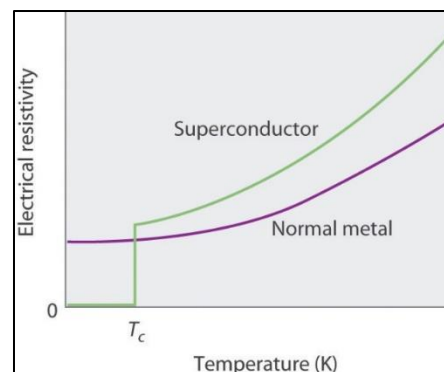


Figure 1-1. Superconducting electrical resistivity and critical temperature [3].

Superconducting electronics are practically difficult to implement. The low temperature requirements are a main barrier of entry. In order to maintain these superconducting electronics in an operational state, cryogenic systems must be integrated with the electronics. This adds additional complexity, as cryogenic systems are difficult to implement and heat lift at very low temperatures is notoriously difficult to achieve efficiently. In order to design these systems, thorough knowledge of the electronics packaging's thermal behavior at cryogenic temperatures is necessary.

1.2 Contributions of Current Work

Northrop Grumman Corporation (NGC) is currently designing superconducting computers utilizing a niobium-based superconductor. These systems require careful consideration of thermal management due to this superconductor's limited operational temperature range. For these systems, the microchips must be kept in an operational window of 4 to 4.5 Kelvin in order to maintain reliable superconducting properties. In designing the cryogenic packaging and housing for these microchips and the associated cryogenic cooling system, a detailed knowledge of the thermal conductivity associated with the materials that make up the heat path between the heat generating chips and cooling system must be reliably and accurately known. Because of the cryogenic temperature range, these systems are kept in vacuum to minimize parasitic heat loads and rely on conduction heat transfer to lift heat from the chips to the cooling system.

This work revolves around the characterization of a set of materials for use in thermal applications for cryogenic superconducting electronics, specifically in relation to the NGC operational requirements and in the temperature range of interest around 4 Kelvin. The main objectives of this work are to provide robust material thermal contact resistance data with surface topography, roughness, and pressure application data for effective and reliable cryogenic packaging solutions for these superconducting electronics and to create a database of relevant properties for high fidelity thermal modeling. The main property of interest is thermal conductivity, and the material of interest is oxygen-free high thermal conductivity (OFHC) copper. The thermal contact resistance that is associated with interfaces between these materials under various conditions is difficult to quantify repeatedly and with high confidence. The

goals of the research are to find high conductivity solutions for material selection as well as packaging solutions that will allow the reliable formation of low resistance thermal contacts in order to maximize the ability of a cryogenic system to achieve very low temperatures at the microchips in a reliable and efficient way.

The main goal of the experimental work is to fabricate and commission a test facility for measurement of bulk and contact thermal conductance in the temperature range of interest. With this facility, characterization of vendor caused variability in material bulk conductance is tested in order to provide quantitative data related to vendor performance and reliability for application in finalized packaging solutions. This work also focuses on characterizing inherent measurement variability and repeatability of dry-contact thermal contact resistance measurements as well as the influence of thermal interface materials (TIMs) and other factors such as applied pressure and surface roughness on contact resistance. These measurements quantify margins of uncertainty in packaging resistances and help to develop appropriate methodologies for high conductivity thermal contacts. They also characterize the necessary performance margins to use when designing contacts that must be repeatedly demounted.

1.3 Thermal Contact Resistance/Conductance

Contact resistance is the thermal resistance associated with the non-ideal surface mate between two bulk materials. There are two main contributors to contact resistance: constriction and boundary resistance. While surfaces can appear macroscopically smooth and flat, in reality the surfaces have innate roughness and microscopic imperfections. Asperities along the surfaces cause uneven contact and conduction through small points of contact where these high points meet, as can be seen in Figure 1-2. Interstitial gas can transfer heat through convection in contacts, but in vacuum systems convection is not an available heat path as there is effectively no gas for convection to occur through and the heat flux must nominally travel only through radiation or conduction through the effective points of contact that cause a heat flow constriction. In addition, if the mate is made for two differing materials, there will be an inherent interface resistance at the contact due to the mismatch of the energy carriers of the two materials.

This resistance, also commonly referred to as boundary resistance, is present even in ideally flat mates and is dependent on the percentage of heat carriers that can transmit across the physical boundary of the materials [4].

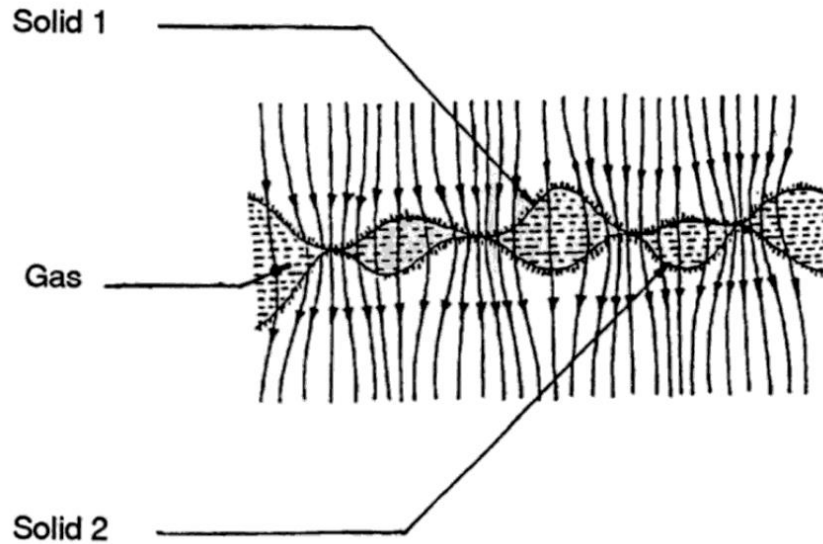


Figure 1-2. Asperities and heat flow paths through a pressed contact [5].

Because there is additional resistance due to the imperfect contact between surfaces and reduced area for heat transfer, there will be a temperature drop associated with this additional resistance that appears to occur in a region that is very thin and adjacent to the contact. The resistance for a given contact can be expressed as

$$R_c = \frac{\Delta T}{Q} \quad 1-1$$

where R_c is the contact resistance, expressed in K/W for a given apparent contact area, ΔT is the temperature drop across the contact and Q is the heat flow rate. A visual representation of this contact resistance temperature drop can be seen in Figure 1-3 in which the bulk materials exhibit a linear temperature profile for conduction and an additional temperature difference can be observed at the contact.

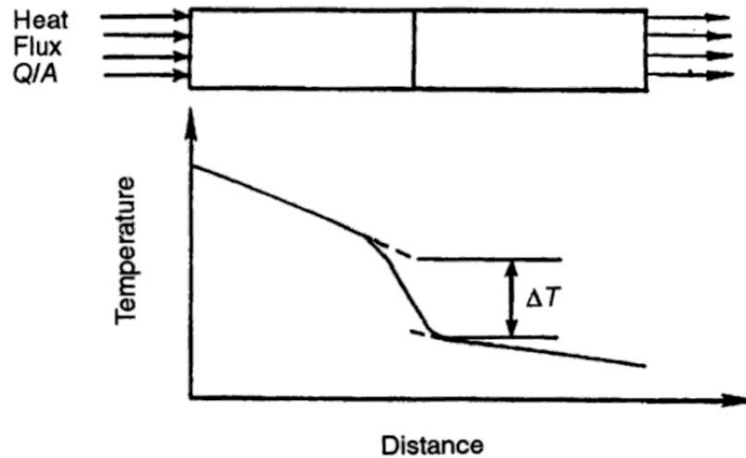


Figure 1-3. Temperature distribution across materials and contact for a steady state heat flux [5].

Thermal contact resistance is commonly experimentally reported in terms of K/W instead of unit-area specific resistance, in units K-m²/W, due to common issues of repeatability for contact resistance measurements in differing conditions. For our purposes we will be utilizing the unit area-specific resistance in order to present data that is generally useful. The area-specific thermal resistance is notated as R'' which has units K-m²/W. The definition of this parameter is given in equation 1-2 where A_c refers to the nominal (macroscopic) contact area, rather than the true (microscopic) contact area.

$$R'' = R_c * A_c = \frac{\Delta T * A_c}{Q} \quad 1-2$$

The resistance can also be expressed in terms of thermal conductance with the relation:

$$G = \frac{1}{R_c} = \frac{Q}{\Delta T} \quad 1-3$$

where G is the thermal conductance of a contact in units W/K. Resistance and conductance are both commonly used metrics to present experimental data for thermal contacts and represent the same effect.

2 Literature Review

2.1 Cryogenic Bulk Thermal Conductivity

In experimental characterization of cryogenic bulk conductivity, measurements are commonly performed by applying a known heat transfer rate across a material and measuring the temperature difference across a known length on the axis of heat flow [6]. Thermal conductivity is then derived from Fourier's Law,

$$\kappa(\bar{T}) = \frac{L\dot{Q}}{A\Delta T} \quad 2-1$$

where $\kappa(\bar{T})$ is the temperature dependent thermal conductivity in W/m-K, L is the axial length between temperature measurements, \dot{Q} is the heat applied, A is the cross-sectional area through which the heat flows, and ΔT is the temperature difference between the two measured points [6]. It is important to note that for these conductivity measurements, if the temperature dependent thermal conductivity experiences large fluctuations over the temperature range of interest, the temperature difference measured must be small enough to represent differential temperature difference at the average temperature of interest. Otherwise, the conductivity measured becomes the integrated average of the conductivity over the range of temperatures between the two sensors and is not an accurate representation of the true conductivity. At cryogenic temperatures, the materials we are testing (e.g., copper) commonly have thermal conductivities with a strong temperature dependence, shown in Figure 2-1.

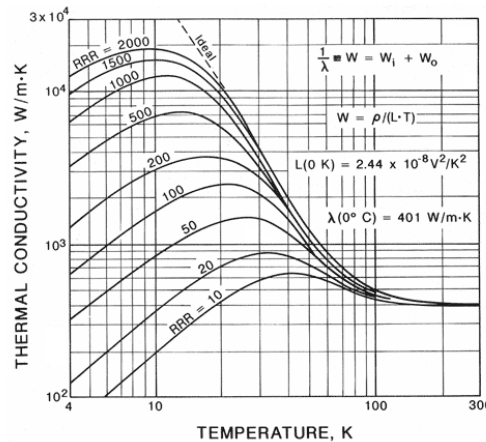


Figure 2-1. Cryogenic thermal conductivity of copper [7].

In order to perform these measurements at cryogenic temperatures, typically a sample is mounted to a cryostat of some kind and shielded from thermal radiation. One high precision experimental apparatus designed by Tuttle et. al at the NASA Goddard Space Flight Center for this type of testing can be seen in Figure 2-2. A sample is mounted with temperature sensors and heaters on a cold plate apparatus for high precision conductivity measurements [6].

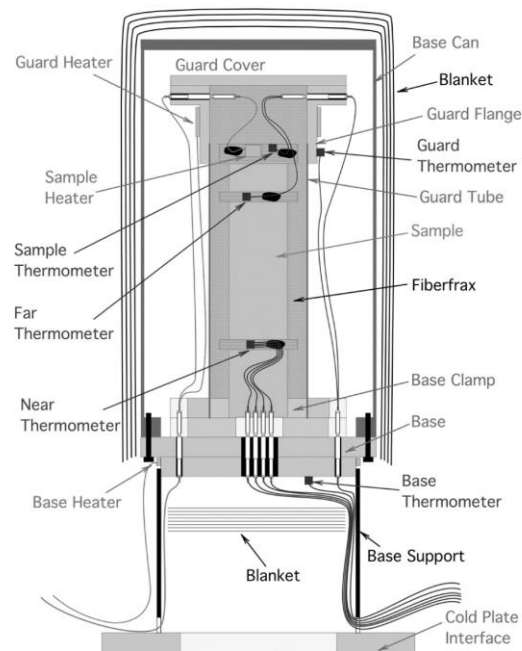


Figure 2-2. NASA Cryogenic Thermal Conductivity Test Apparatus [6].

As can be seen in the figure, in cryogenic thermal measurements, careful consideration must be taken to minimize thermal radiation as well as to carefully control the temperatures at each end of the test sample. It is important to keep a heater on not only the sample where heat will be supplied for testing, but also on the base to ensure the average temperature of the sample can be well controlled, especially for cryocooler cold plate systems where the cold plate temperature is regulated only by heat load. The researchers also utilized a guard to reduce any radiative heat leak between the sample and its surroundings. Additionally, in the figure it can be seen that the researchers took care to heat sink all electrical wires entering the apparatus to ensure that the wiring does not create parasitic heat leaks to the sample. Due to the importance accounting for all of heat sources in thermal conductivity experiments,

reducing parasitic heat leaks is one of the most important experimental factors to ensure precise and accurate measurements.

2.2 Cryogenic Thermal Contact Resistance

In past research, thermal contact resistance at low cryogenic temperatures has been measured in a variety of experimental configurations that depend on the researchers' specific materials and applications of interest. Generally, the samples are mounted in a cryostat and pressed together with a force applying apparatus. In most methodologies, researchers measure the temperature drop across the contact point and the heat flux applied to the contact to calculate the associated resistance. The most relevant historical research is discussed below.

At UW–Madison, cryogenic thermal conductance characterization was carried out in 1984. Van Sciver et. al performed simultaneous thermal and electrical contact conductance measurements for copper tube stock samples pressed together using a stainless-steel compression spring force assembly, shown in Figure 2-3 [8]. In this experiment, the force was not changed, and the spring provided a nominal 90 N force translating to a 9 MPa contact pressure on the samples. Their findings for thermally conductive metallic contacts were that the best conductive contacts are achieved with pure soft metal TIMs such as indium [8].

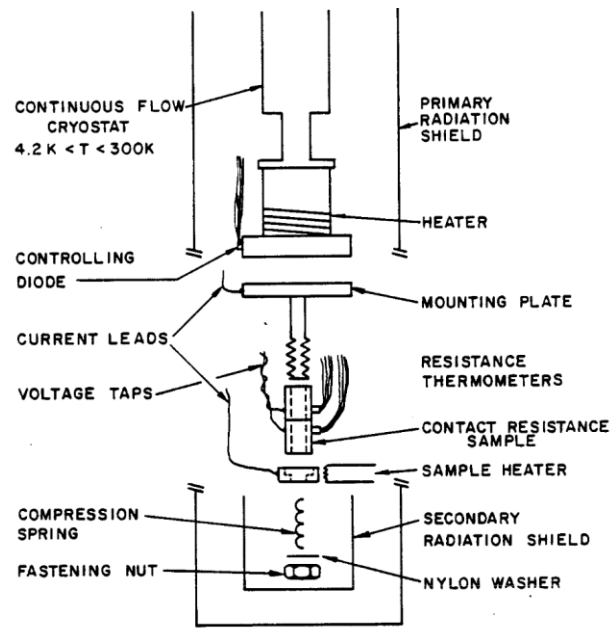


Figure 2-3. Van Sciver et al. experimental apparatus [8].

In 1998, Gmelin et. al [9] reported data on thermal contact resistances between copper, steel, and copper-steel contacts with a range of thermal interface materials from room temperature to roughly 10 Kelvin. To make their measurements, a sample holder was mounted to a test platform in a continuous flow cryostat and a spring force head was utilized to press the contact, very similar to the UW–Madison experimental apparatus. They found in their testing that high pressure, clean surfaces free of oxides, and thin TIM applications resulted in the lowest thermal contact resistance measurements. They also found that of the TIMs that were tested, indium and Apiezon-N thermal grease resulted in the lowest contact resistances.

In an expansion of this earlier data, Ram Dhuley at Fermilab in 2019 provides a current and in-depth survey of thermal contact resistance data, test methodologies and theoretical models for pressed dry copper and gold-plated copper contacts [4]. The main data range of interest for this review was conduction cooled cryogenic systems at or below 4.2 Kelvin, and the results were compiled with all available information on contact area, applied force, surface roughness, etc. made available by past researchers. Included in Dhuley’s survey of data is the research from Northrop Grumman that precedes this current work.

At NGC, Dillon et. al performed contact conductance measurements for OFHC copper dry contacts with a variety of TIMs for application to superconducting electronics cryogenic packaging [10]. This work was performed with a piece of bulk material that mounts directly to the cold surface, defined as an interposer by the researchers, and a block of bulk material that was mounted with a force head that bolted to the interposer, applying the force to the contact as shown and labeled in Figure 2-4. Temperature sensors were mounted to the interposer and the bulk material block and the temperature difference across the contact was measured. The bulk material resistance between the temperature sensor mounting locations and the contact was corrected for through calculation using assumed bulk conductivities. The heat transfer across the contact was determined through 4-wire measurement from the heater element which gave the total heat dissipated by the heater element. To isolate the heat that flowed through the contact, the heat leak through the alternate heat flow path associated with the force head was corrected for through calculation with the thermal resistance of the force head pathway determined using ANSYS modeling.

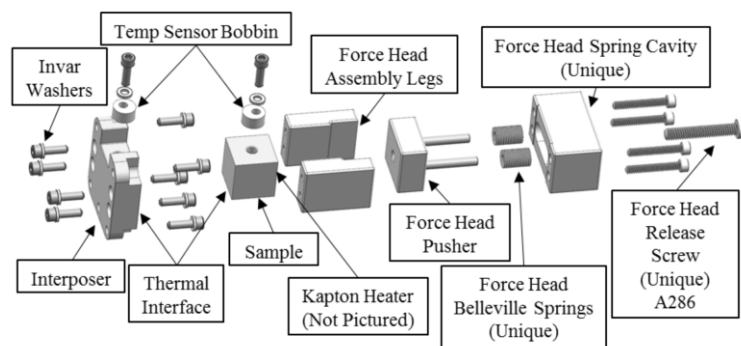


Figure 2-4. Contact sample holder in historical Northrop Grumman testing [10].

In the past NGC testing, the relevant forces tested for the electronics packaging were 62.3 N and 458.4 N for a contact surface area of 2.32 mm^2 . These forces were nominally chosen to simulate the possible mounting applications that could range in force from 44 N to 445 N. The true applied forces of 62.3 N and 458.4 N were calculated from experimental data obtained with a load cell at room temperature and corrected for changes in the force that occur due to thermal contraction and changes in the spring stiffness of the Belleville springs used in the force head. It should be noted that the force applications had

to be separately tested on physically different contacts as each force required a different force head configuration. They found that at the higher applied force, the indium foil TIM produced the highest thermal contact conductance, and that at the lower applied force the indium and gold-plated surfaces both performed well and were comparable. In continuation and improvement of this research, the current work will expand on the characterization of variability in contact resistance for an array of material, TIM, and influencing factor combinations and also explore the repeatability of these measurements.

The other research that provides a reference for this work was carried out at the Ames Research Center to characterize thermal contact conductance. A fairly large database of material contact conductance relevant to our current investigation was experimentally quantified, and Salerno and Kittel summarized the available cryogenic thermal contact conductance literature in addition to all of the research performed and compiled by their research group in a technical memorandum [11]. Their tests were performed over the temperature range of 1.6-4.2 Kelvin and with applied forces ranging from 22 to 670 Newtons. Measurements were made with two temperature sensors measuring the temperature difference across a contact while a heat load was applied, and corrections were made for the bulk material resistance between the sensors and the contact that contribute to the overall measured resistance. The materials tested included copper, aluminum, brass and stainless steel. Gold plating, indium foil, and Apiezon grease were included in the TIMs that were tested in addition to dry contacts over ranges of applied force. The forces were applied in Salerno and Kittel's experiments with a rocker arm, pictured in Figure 2-5, that was actuated using a wire connected to an external motor and load cell [12].

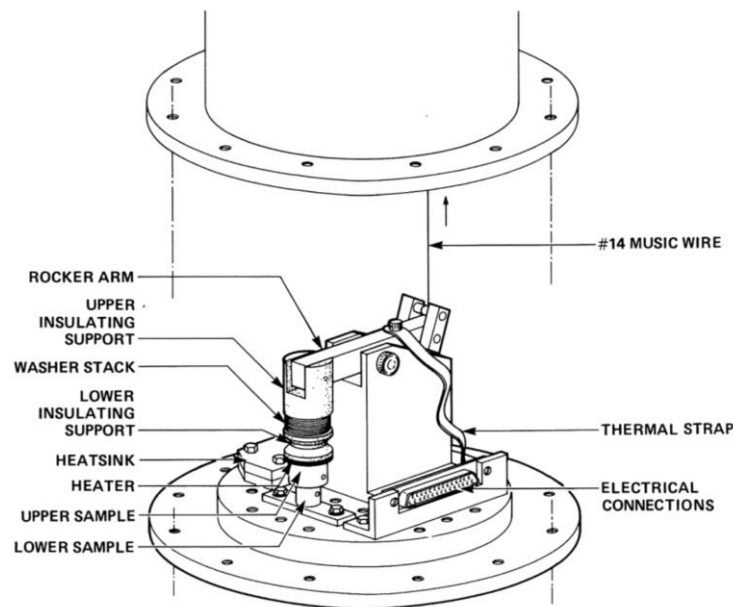


Figure 2-5. Salerno et. al contact conductance experimental apparatus [12].

This unique force application method allowed for in-situ force application at the temperatures of interest, in contrast to the NGC force head method where the force had to be applied at room temperature between tests. Applying the increased force to the contact in incremental steps without breaking the contact ensures that the force and contact resistance relationship is measured independent of other variabilities that are associated with making a contact; but it is also somewhat inconsistent with how force is applied in a typical application. The in-situ force application increases contact resistance through increasing the contact area as the materials continuously deform. This approach cannot be assumed to quantitatively perform in a way that is equivalent to force applied at standard atmospheric temperature conditions. For the applications being considered by the present study, a cryogenic packaging assembly would be carried out in standard conditions and not at cryogenic temperatures.

From their experimental data, Salerno and Kittel found that “conformal coatings” of indium and Apiezon thermal grease resulted in the highest conductance contacts, which agrees with findings from Gmelin et. al and Dillon et. al [11]. For aluminum, brass and copper contacts, they found that Apiezon was better at improving conductance than indium, although both still greatly improved the performance relative to dry contacts. In terms of force, their data showed that conductance as a function of force

appears to follow a power law relationship but can vary greatly depending on the inclusion of different TIMs. For example, in the brass, copper and aluminum contacts with the indium and Apiezon TIMs, the conductance data was largely independent of applied force. This is likely due to the initial, low force being sufficient to create the conforming contact.

2.2.1 Sources of Variability in Contact Resistance

In general, factors that can affect the thermal resistance of a contact include contact pressure, bulk material properties (elasticity and hardness, energy carrier characteristics that lead to bulk conductance), surface roughness and machining, surface cleanliness and the presence of oxide layers, and the use of TIMs. There is also inherent variability in contact resistance due to the non-uniform nature of making contacts and the difficulty of creating uniform and repeatable conditions under which to make contacts. As discussed in this literature review, general results of cryogenic contacts show that clean surfaces, fluid or soft, thin conforming layers of TIMs, and reduced surface roughness all contribute to reducing thermal resistance [9].

2.3 Theoretical Models for Contact Resistance

There are a large number of physics-based models that have been proposed to estimate and predict contact resistance. Most models account for both the constriction and thermal boundary resistances, using varying methodologies that depend on the materials that make the contact. The main model described and used for correlation comparisons in this research will be a combination of a thermal constriction resistance model and diffuse mismatch model (DMM) compiled by Ram Dhuley for Fermilab [4]. This model was chosen for use in correlations as it was developed for cryogenic metallic contacts that are relevant to our materials and contacts of interest.

2.3.1 Thermal Constriction Resistance

In modeling thermal constriction resistance, Dhuley utilized a model derived from unifying the mechanics, thermal analysis and deformation that occur in a contact. In terms of deformation, plastic contacts are assumed because (as noted by Dhuley) Greenwood (in [5]) showed that new contacts made

with even very small contact pressure will deform plastically. The relation for the true contact area from the apparent contact area and contact properties is given by [5]:

$$\frac{A_p}{A_a} = \frac{p_{app}}{H_c} \quad 2-2$$

where A_p is the true physical contact in m^2 , A_a is the apparent contact in m^2 , p_{app} is the applied contact pressure in Pa, and H_c is the surface microhardness in Pa.

Utilizing this relation for true contact area given the conditions of the contact, the thermal constriction resistance can be derived and expressed as:

$$R''_{BC} = \frac{1}{A} \left(\frac{\sigma_s}{m_s} \right) \frac{1}{k_s} \left(\frac{p_{app}}{H_c} \right)^{-B} \quad 2-3$$

where R''_{BC} is the constriction resistance in $K \cdot m^2/W$ in terms of the apparent contact area, σ_s is the equivalent mean surface roughness in m, m_s is the equivalent mean slope of asperities in radians, k_s is the equivalent thermal conductivity of the two bulk materials, and A and B are numerical constants that vary slightly dependent on the theoretical model assumptions [4]. The constriction resistance represents the additional thermal resistance due to the reduced contact area through which the heat flux can flow.

Assuming Gaussian roughness on the surfaces, the equivalent mean surface roughness and equivalent mean asperity slope can be found with equations 2-4 and 2-5 respectively, where the subscripts 1 and 2 refer to the two surfaces making contact. The mean surface roughness and mean slope of asperities can be found experimentally. The equivalent thermal conductivity can be found using the two bulk materials conductivities given by Madhusudana [5] in equation 2-6.

$$\sigma_s = \sqrt{\sigma_1^2 + \sigma_2^2} \quad 2-4$$

$$m_s = \sqrt{m_1^2 + m_2^2} \quad 2-5$$

$$\frac{1}{2k_1} + \frac{1}{2k_2} = \frac{1}{k_s} \quad 2-6$$

For a variety of models, the numerical constants A and B vary dependent on the conditions of the regime of interest. For this model, the numerical constants A and B are taken from Yovanovich to be $A=1.25$ and $B=0.95$, which were found to correlate to relevant experimental data most closely [13].

The required quantitative data to determine a contact's constriction resistance include the bulk material's hardness, bulk conductivity, the applied contact pressure, the surface roughness and asperity profiles, and the apparent contact area. For our contact measurements, surface imaging and experimental measurements of sample bulk conductivities in-situ during contact resistance measurements are recorded and allow us to compare with this model.

2.3.2 Boundary Resistance

For the thermal boundary resistance, Dhuley utilizes a diffuse mismatch model (DMM) developed by Gundrum et. al for the diffusion of electrons across metal-metal contacts [14]. From this model he derived the expression for a perfect contact resistance, in which the apparent contact area is equal to the true contact area, to be:

$$R''_{BD}(T) = \frac{16E_F}{\pi^2 k_B^2 n_e v_f} T^{-1} \quad 2-7$$

where $R''_{BD}(T)$ is the temperature dependent boundary resistance in K-m²/W, E_F is the Fermi level heat carrier energy in Joules, k_B is the Boltzmann constant, n_e is the conduction electron density in 1/m³, v_f is the Fermi level heat carrier velocity in m/s, and T is the temperature in Kelvin. In order to apply this to a real contact, the relation in equation 2-2 is utilized to find the pressed contact resistance to be:

$$R''_{BD}(T) = \frac{16E_F}{\pi^2 k_B^2 n_e v_f} T^{-1} \left(\frac{p_{app}}{H_c} \right)^{-1} \quad 2-8$$

where $R''_{BD}(T)$ is the temperature dependent boundary resistance in K-m²/W for a given apparent area.

2.3.3 Total Contact Resistance Model for Cryogenic Applications

Effectively, the thermal constriction resistance and physical boundary resistance act in series to affect the resistance of a contact. Because of this, equations 2-7 and 2-8 can be summed to express the total thermal resistance of a contact according to:

$$R''(T) = \frac{1}{A} \left(\frac{\sigma_s}{m_s} \right) \frac{1}{k_s} \left(\frac{p_{app}}{H_c} \right)^{-B} + \frac{16E_F}{\pi^2 k_B^2 n_e v_f} T^{-1} \left(\frac{p_{app}}{H_c} \right)^{-1} \quad 2-9$$

where $R''(T)$ is given in units $K \cdot m^2/W$ expressed in terms of the apparent contact area.

Dhuley found that this model qualitatively applied to low temperature behaviors in metallic contact resistances and followed the observed trends of temperature effects in thermal conductivity, with a T^{-1} dependence [4]. He also applied this model to available experimental datasets of copper-copper and gold-plated copper-copper contacts. He found that in all cases considered, both constriction and boundary resistance contributed comparably and were non-negligible resistances in the contacts studied. He also found that experiments on gold-plated contacts also agreed well with the model calculations and concluded that in general the model predicts reasonably well the resistance of metallic contacts. Comparisons of model results for the data presented in this work are analyzed and discussed in Chapter 6.

3 Experimental Apparatus and Design

3.1 Vacuum Chamber and Cryocooler

The facility used for the experimental test apparatus fits within a bell jar vacuum chamber. The chamber is made of 304 stainless-steel with a 30-inch inner diameter and a height of approximately 30 inches, as shown in Figure 3-1. Electrical feedthroughs and the vacuum pump and gauge are integrated with the chamber through KF-40 flanges placed around a bottom ring and any additional openings are sealed with blank KF-40 flanges or conflat.



Figure 3-1. Vacuum Chamber Exterior.

To cool the test samples within the chamber to the required cryogenic temperatures, an RDK-415D Sumitomo cryocooler is installed into the vacuum chamber, as shown in Figure 3-2. The cryocooler is mounted with the cold head stages facing upwards due to the orientation of the available openings in the chamber as well as to allow for easy mounting of the samples and test fixtures. The cryocooler consists of two stages and is connected to a Sumitomo F70L compressor. The cold head is capable of providing a heat lift of 45 Watts at 50 Kelvin on the first stage and 1.5 Watts at 4.2 Kelvin on the second stage.

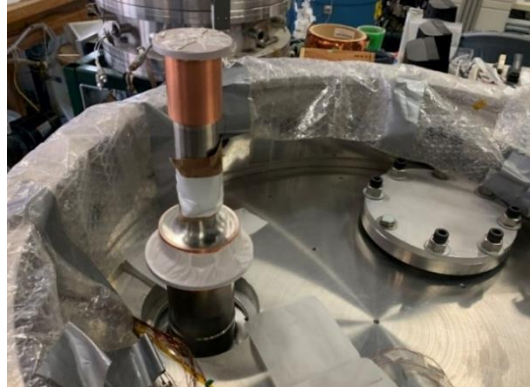


Figure 3-2. Cryocooler mounted within the vacuum chamber.

3.2 Thermal Jackets and Sample Platform Design

In order to reduce radiative heat load and isolate the test stages, thermal jackets were designed to attach to the two stages of the cryocooler, as shown in Figure 3-3. The first stage plate and jacket as well as the second stage jacket are fabricated from 6061 aluminum, and the second stage platform plate is fabricated from 110 copper with stainless steel helicoil inserts to allow for bolting of samples and test fixtures. Copper was chosen for the sample platform because it exhibits higher thermal conductivity than aluminum. The size of the thermal jackets was determined based on the available space and mounting options within the vacuum chamber and to allow for the possible mounting of multiple samples. Drawings of these components can be found in the appendix.

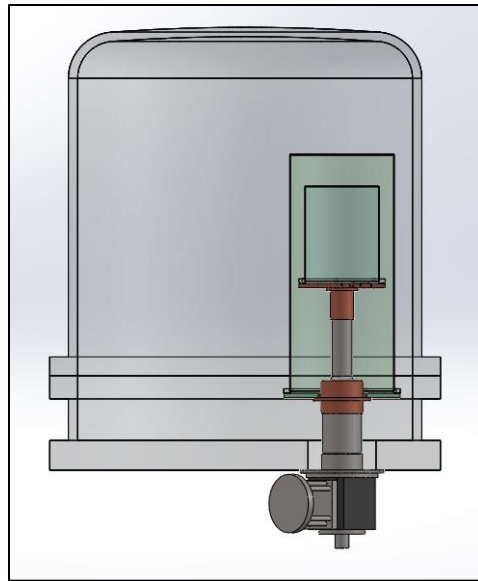


Figure 3-3. Thermal jackets mounted in bell jar on Sumitomo cryocooler.

These thermal jackets reduce parasitic heat leak on the second stage cold head by thermally isolating each stage from the warmer surroundings, reducing the radiative heat load that the samples will see. It was important to minimize the external heat load on the second stage in order to maximize the heat that could be applied to the test sample which, in turn, increased the temperature difference and improved the accuracy. As we were limited by the maximum heat lift available from the cold head, any additional heat loads affected our ability to test at higher heat inputs. The first stage and second stage plates and their attached jackets were also designed to allow for easy pass through of wiring and mounting of heat sink bobbins as well as to facilitate mounting test fixtures on the second stage.

3.2.1 Thermal Contraction Considerations

When designing the thermal jackets, thermal contraction was an issue that had to be considered. It was important that the second stage jacket, which consisted of an aluminum jacket flange rigidly mounted onto a copper plate, would not be subjected to a large mechanical stress due to the different thermal contraction experienced by the aluminum and copper as they cooled to cryogenic temperatures. To understand the mismatch in thermal contraction, a simple linear thermal contraction calculation was performed for the copper and aluminum second stage thermal jacket pieces. Linear thermal expansion or contraction can be found from the equation:

$$\Delta L = L_0 \alpha (T_1 - T_0) \quad 3-1$$

where ΔL is the change in length, L_0 is the initial length at temperature T_0 , T_1 is the final temperature, and α is the temperature integrated averaged linear expansion coefficient of the given material. This was the equation utilized for copper thermal contraction, and the value of α was calculated through integration within MATLAB utilizing the linear thermal expansion coefficient equations for the relevant temperature ranges available through NIST [15]. For the aluminum 6061, thermal contraction was calculated from dL/L , given also through NIST reference [16]. For the 8-inch (20.32 cm) outer diameter second stage jacket flange and platform plate, the cooling of the plates translates to a contraction from room temperature to 4 Kelvin of 0.069 cm for copper 110 and 0.084 cm for aluminum 6061. It was determined

that the differential contraction of 0.15 mm was nominally inconsequential and could be adequately dealt with by the bolt stress.

3.2.2 Sample Platform Design

The second stage plate attaches to the thermal jacket and also acts as a mount for the test fixtures. Copper was chosen over aluminum for this piece for its higher thermal conductivity at the temperatures of interest. A linear bolt pattern was chosen to allow for flexibility with regard to mounting configurations and provide the possibility to mount multiple test fixtures to run during one test. This pattern can be seen in Figure 3-4. The pattern distance and bolt sizes were selected in order to ensure that the stage would be compatible with test fixtures that have previously been tested and will be used for commissioning.

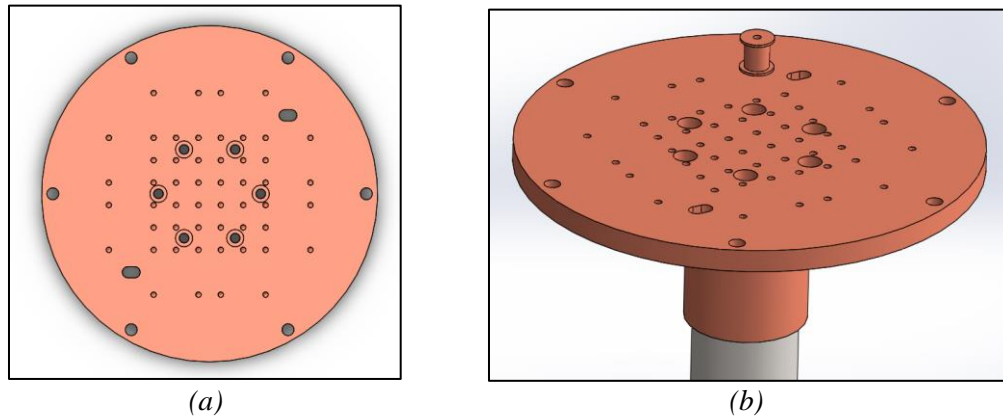


Figure 3-4. Second stage copper sample plate.

The platforms for the thermal jackets that were fabricated and mounted in place can be seen below in Figure 3-5 with bobbins installed for thermal sinking wire leads. These platforms were mounted to the cryocooler interfaces with indium gaskets to reduce the thermal contact resistances.



Figure 3-5. Thermal jacket platform plates installed onto cryocooler.

3.3 Liquid Helium Dampening Pot and Revised Design

While initially commissioning the test facility, it was observed that large thermal oscillations occurred at the second stage cold head. These arise due to the thermodynamic cycle associated with the Gifford-McMahon cryocooler. The oscillations varied with average temperature but were observed to be roughly 0.2 K peak-to-peak at a frequency of 1 Hz for a stage temperature of ~ 3.5 K, as seen below in Figure 3-6.

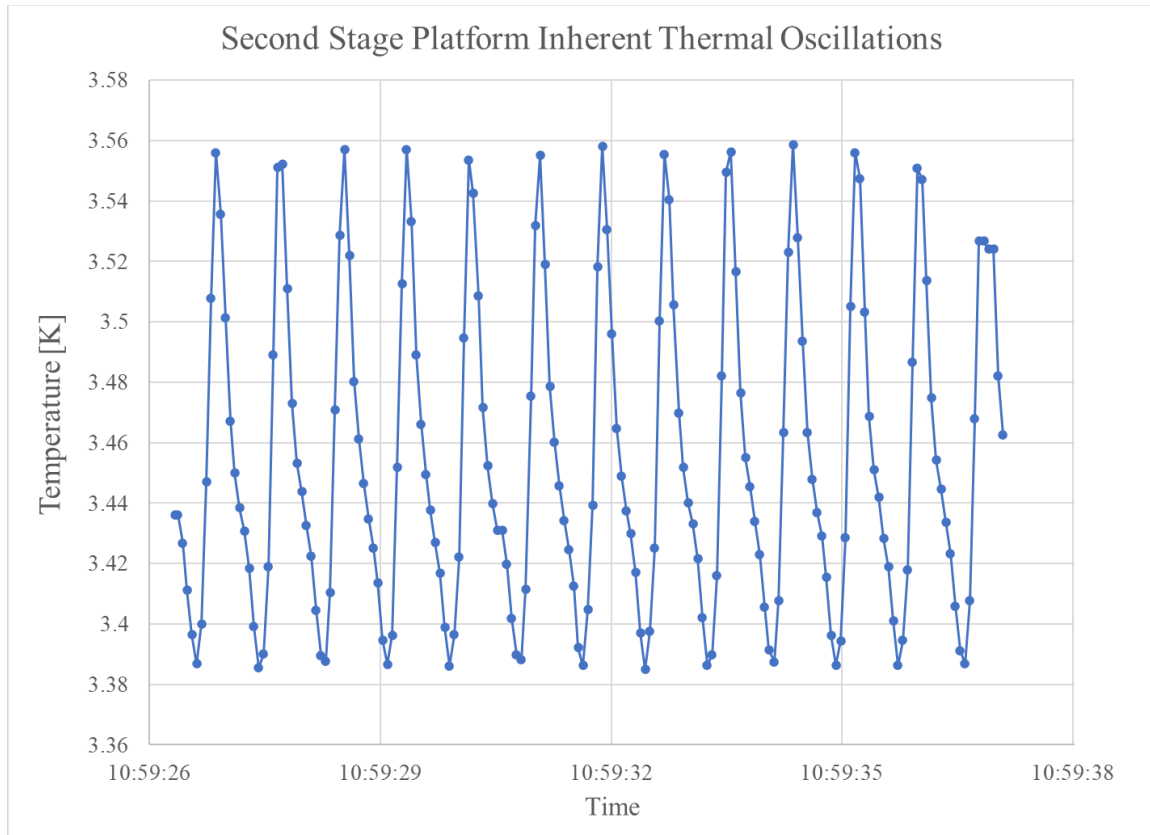


Figure 3-6. Inherent thermal oscillations on testing platform on GM cryocooler.

These large thermal oscillations introduce an additional uncertainty in the steady state data collected due to the transient conduction effect in the sample. By taking large collections of data samples and averaging them, this error can be reduced but the impact of the transient thermal wave on the results introduced uncertainty that was better avoided. To conservatively estimate the potential impact of these oscillations we included the magnitude of the oscillation as a random uncertainty in the bulk and contact resistance measurements. This approach suggested that oscillations on the order of magnitude of tens of millikelvins up to about 0.1 K are acceptable and keep the overall uncertainty of bulk conductivity measurements below 10%.

To dampen these oscillations to within this designated acceptable range, we designed a liquid helium dampening pot to sit within the second stage and act as thermal mass to reduce the oscillations. Liquid helium was chosen as the thermal mass due to its very high relative heat capacity at the target temperatures in comparison to other available options such as copper. Liquid helium dampening pots are

available commercially for cryocoolers but due to lead time, integration, and cost restrictions, we designed and fabricated our own system. The design of this system can be seen below in Figure 3-7.

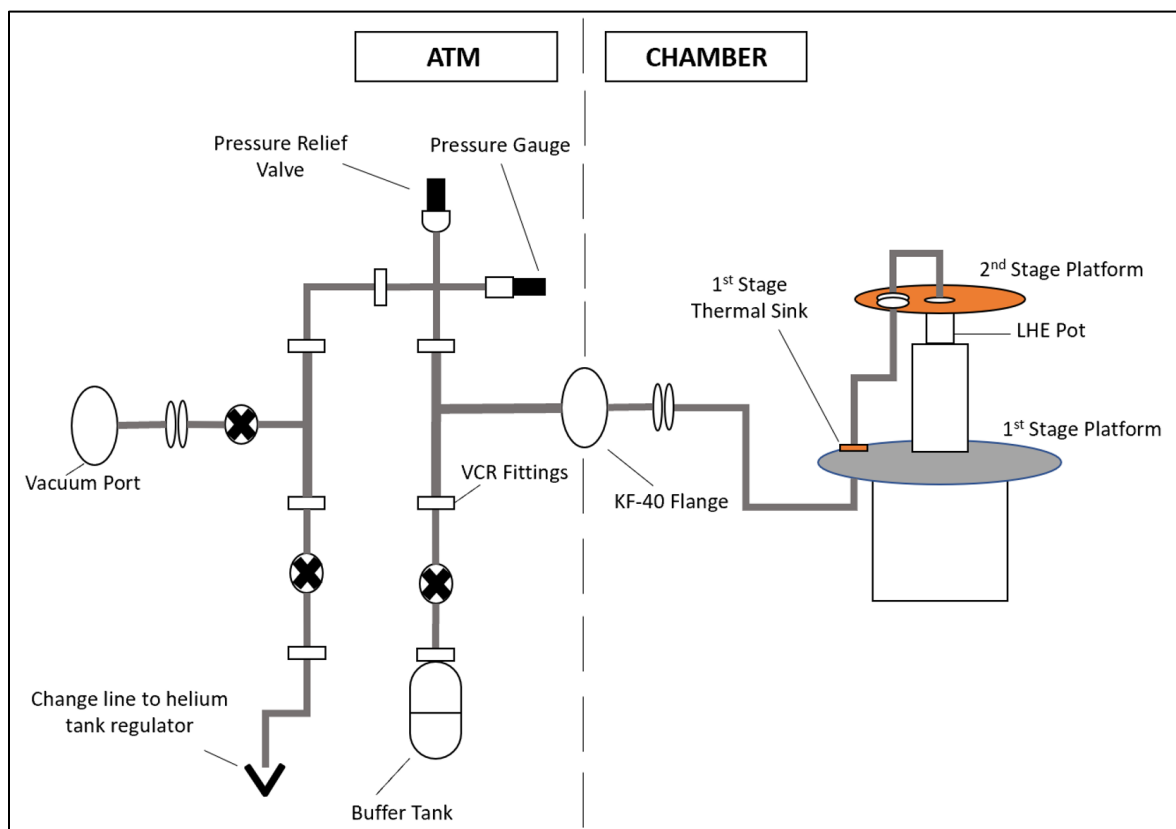


Figure 3-7. Liquid helium dampening pot system.

The main elements of the liquid helium dampening pot system are a buffer tank, heat sunk piping, and a small pot that is attached to the cryocooler. The piping and tanks are evacuated and charged with helium, and then the system operates in a closed loop, meaning no additional helium must be added and no procedural steps must be taken to operate the system during a test cycle as it passively functions. When the cryocooler is turned on and reaches liquid helium temperatures, the helium within the dampening pot itself liquifies providing the large heat capacity necessary for the thermal dampening. The buffer tank sits outside the vacuum chamber and at room temperature, while the piping connects it to the dampening pot. The purpose of including the buffer tank is to minimize the required charge pressure. Because the system is closed, at room temperature it must be charged to a higher pressure to account for the drop in pressure that occurs once the helium in the dampening pot liquifies. If a buffer tank were not

included, the necessary charge pressure of the helium dampening pot itself would be extremely high; with the buffer tank, the system at room temperature is charged to 200 PSIG.

In fabricating and assembling this design, it was necessary to modify the original sample platform to accommodate the liquid helium pot and work around existing design limitations. For example, a 1-inch flange was added to the outer first stage thermal jacket to raise its height and make room to shift the inner jacket upwards with the addition of the liquid helium pot. Piping was also fed through the second stage platform due to limitations with effectively brazing the piping to the helium pot. For the system outside the vacuum chamber, VCR and NPT fittings were utilized. The elements of this outer system can be seen below in Figure 3-8.

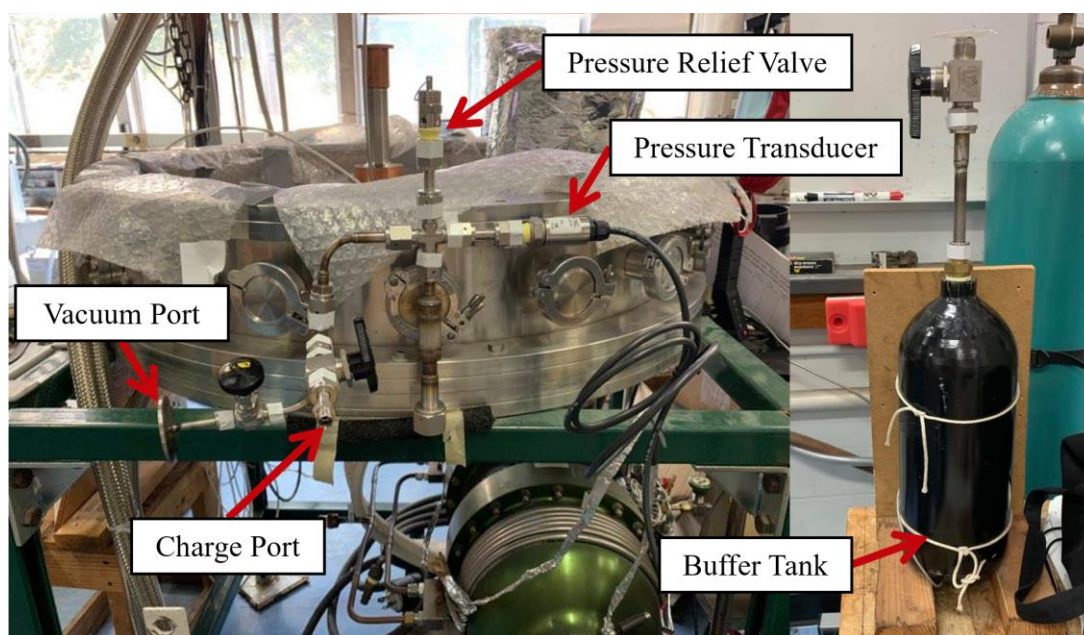


Figure 3-8. Dampening system elements outside vacuum chamber.

All piping within the vacuum chamber was assembled with VCR fittings to minimize any possible leaks and the helium pot itself was constructed from copper and brazed together. This process required substantial trial and error as well as extensive leak testing. Originally, the pot was mounted on the second stage instead of being in series, but this approach did not provide adequate thermal dampening. Additional difficulties with brazing the copper pot itself to be helium leak tight were encountered several times. In the end, the pot was brazed and found to be leak tight, mounted in series with the platform as

shown in Figure 3-7, and additional C101 thermal straps were included. These thermal straps were added because the brazed pot in series with the second stage introduced extra thermal resistance that raised the no load temperature of the second stage. The system before and after the thermal straps were installed for the final iteration of the design be seen below in Figure 3-9.



Figure 3-9. Helium pot before and after thermal strap installation.

After finalizing the system, ensuring the lines were leak tight and the sample stage was reaching a sufficiently low temperature with the utilization of thermal straps, we found that the oscillations on the stage were very effectively dampened. An example of the oscillations that we saw in testing after this for a bulk conductivity measurement can be seen below in Figure 3-10. The measurements of the two temperature sensors mounted on a bulk conductivity saw peak-to-peak oscillations of ~ 0.02 K or 20 millikelvin, well within the desired dampening range. With this validation, the dampening system was placed into operation. It continually and passively dampens the thermal oscillations within the test rig.

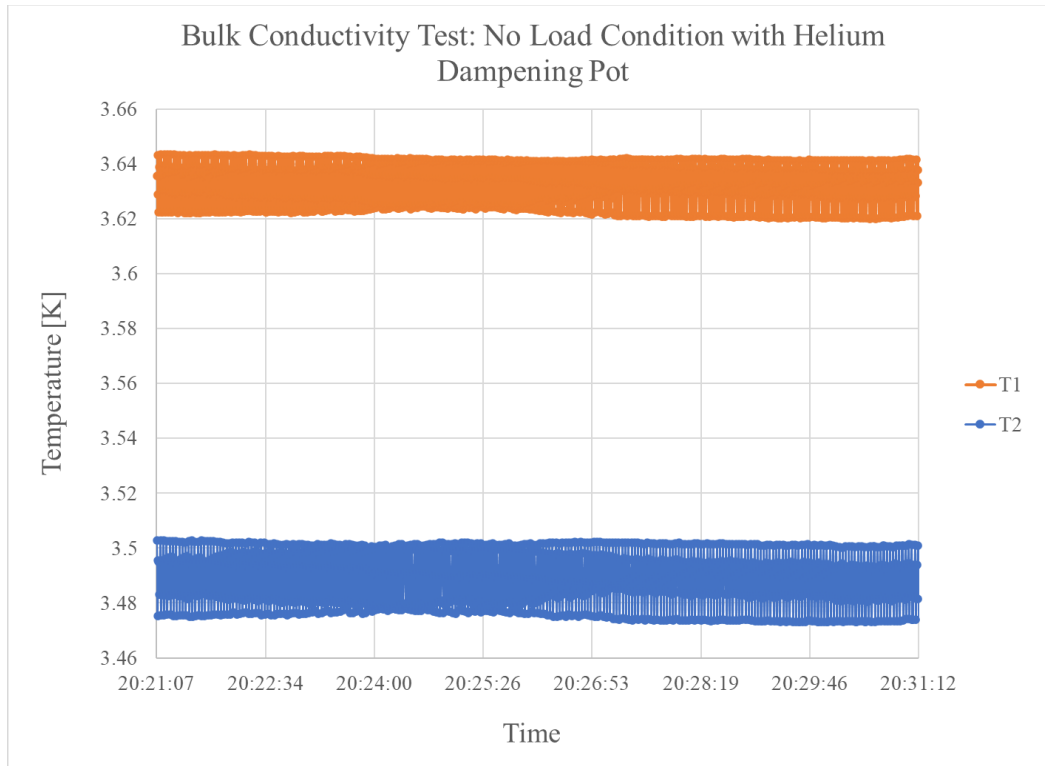


Figure 3-10. Dampened thermal oscillation results.

3.4 Bulk Conductivity Test Fixture

In our characterization of materials, bulk conductivity was a metric of interest due to the uncertainty related to vendor-to-vendor variations. In order to measure and provide quantitative vendor information, bulk conductivity measurements were undertaken before contact resistance measurements were run. The samples and test fixtures for testing bulk conductivity were based on a Northrop Grumman T-beam test fixture used in previous work. This fixture, shown below in Figure 3-11, consisted of a solid single piece of bulk material that was machined into the T-beam shape. Temperature sensors were attached in bobbins that were mounted directly onto mounting holes in the beam, and a heater that supplied a known heat flux was clamped at the top of the beam.

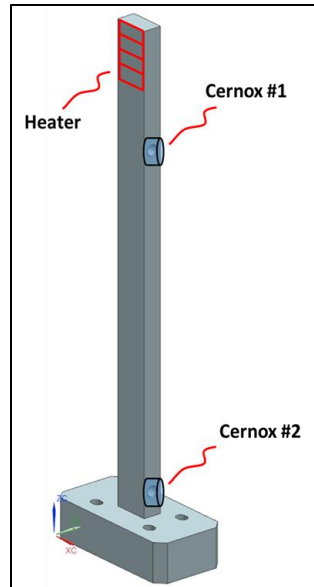


Figure 3-11. NGC T-beam design.

The fixture was redesigned in order to include a few key improvements that allow for reliable and accurate results as well as to ease the testing process. The redesigned fixture can be seen in Figure 3-12 and consists of a 1/2-inch rod of the sample material, bolted to the base of the ‘T-beam’. This change was made to allow for cost reduction in purchasing rods versus large bulk blocks of material. In addition, by testing the rods as purchased from vendors and leaving the bulk of the samples un-machined, we were able to assess the bulk conductivity of the material more accurately from the vendor without introducing any additional work hardening effects.

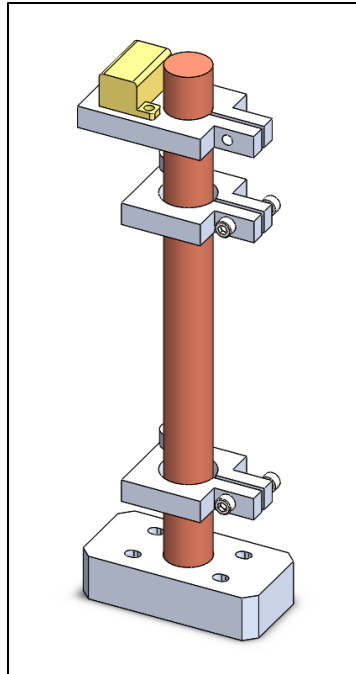


Figure 3-12. Current T-beam design with clamps.

The other main change made was that temperature sensors were moved to mounts with knife-edge clamps instead of directly bolting into the samples. This was done to provide a more precise location of the temperature measurement. In prior designs where the temperature sensors are directly mounted to the T-beam, the holes in which they were mounted disrupted the line of heat flow and the temperature measured was an average over the mounting location. By switching to knife edge clamps, shown in Figure 3-13, the sensors do not affect the sample heat path and also provide a precise location of measurement at the knife-edge. These clamps are made of aluminum and temperature sensor bobbins are mounted directly onto them.

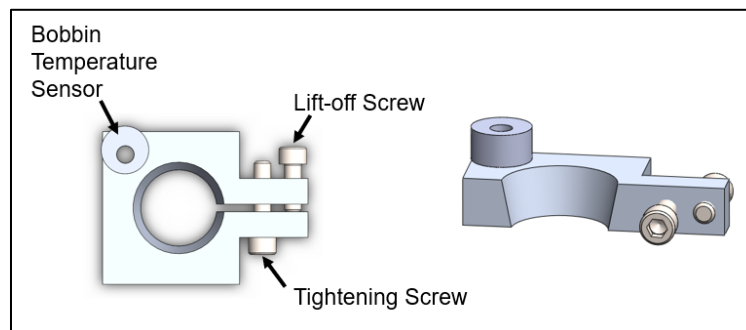


Figure 3-13. Knife-edge clamps.

The heater element, seen in the top of Figure 3-12, was also modified so that it could be attached with a clamp in order to allow the use of cartridge heaters for these tests. The heater clamp is made of copper, again chosen due to its high thermal conductivity. This test fixture along with all clamps were fabricated in-house for all testing.

3.4.1 Temperature and Heat Flux Distribution

To verify that the heater's applied heat flux would flow from the heater through the bulk of the sample in a uniform manner, a simple ANSYS thermal analysis was developed. Copper was used as the sample material in the analysis and steady state conditions with a one-watt heat load from the heater cartridge was set. The base of the mount was held at 4 Kelvin to simulate a constant cold head temperature. As can be seen in Figure 3-15, the temperature distribution becomes even and isothermal perpendicular to the axis of flux above the first temperature sensor placement and the heat flux distribution remains uniform along the area of interest between the two temperature sensors. This confirmed that the configuration for the heater and heat application provides the necessary conditions for the measurements.

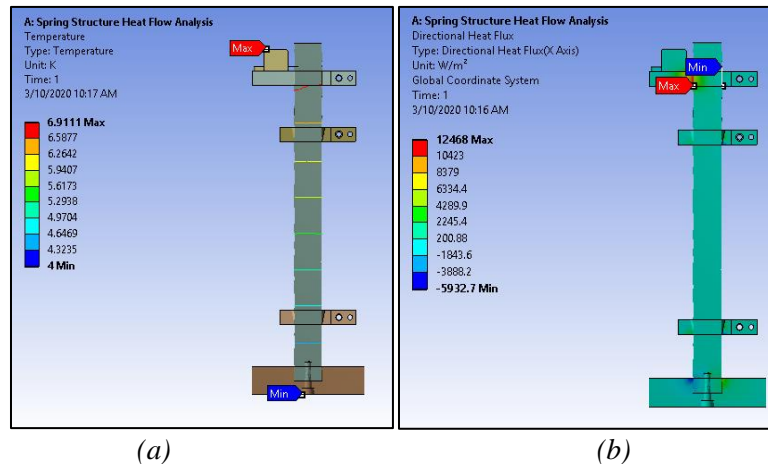


Figure 3-14. Second stage copper sample plate.

3.5 Contact Sample Holder Design

For contact resistance measurements, the test fixture was designed to be compatible with the sample materials tested for bulk conductivity and to allow for evenly applied pressure. The test fixture, shown in

Figure 3-15, was designed to allow force application by tightening a bolt. The contact resistance is measured across the point of contact and four temperature sensors are attached for the measurement along the axis of heat flow. The four measurements allow accurate measurement of the contact resistance by removing the influence of the resistance associated with the bulk conductivity through the sample material that exists between the temperature sensors by measuring directly the temperature gradient in the bulk to allow extrapolation to the temperatures on either side of the contact. This is explained in further detail in Chapter 4 calculations.

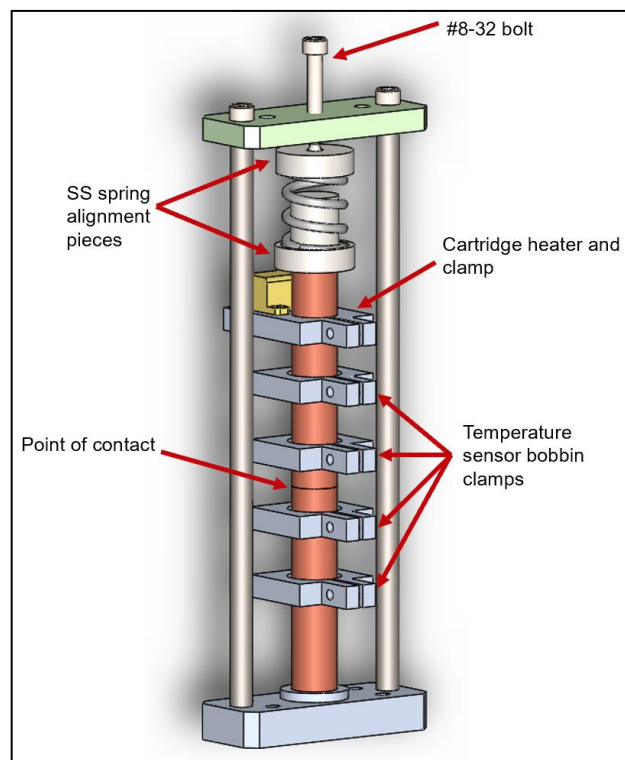


Figure 3-15. Contact resistance measurement test fixture.

For this test fixture, a bolt in the top plate, shown in the figure, is threaded through the top G10 plate (green) and as it is turned, it pushes on the stainless-steel spring to compress it. This style of force application was selected because a large displacement of the spring makes the inevitable displacements related to thermal contractions negligible in terms of their impact on the force. In addition, turning the bolt is a simple method for applying and recording the amount of force applied and it allows for incremental additional force to be added to a contact for multiple measurements. Finally, the method of

application is consistent with most contact holders where the application of force will be applied under room temperature, ambient air conditions and then the assembly subsequently cooled to cryogenic temperatures in a vacuum environment. Stainless steel ball bearings are utilized to provide sufficient mechanical freedom that the contact surface between the samples where resistance is being measured remains flush (square) even in the face of small amounts of non-flatness in the fixture. A center alignment piece keeps the spring straight and aligned to prevent any buckling, as shown in Figure 3-16. As can be seen in this figure, the stainless tubes on either side keep the assembly together and the sample rods sit in collars that help to keep them aligned.

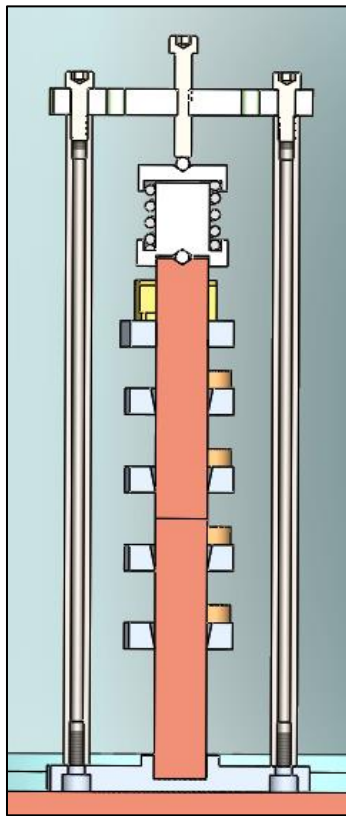


Figure 3-16. Compressed contact fixture with interior view.

As the bolt is turned, the spring is compressed a distance equal to the linear travel of the bolt which can then be translated into force given the spring constant. For example, a #8-32 bolt requires 32 revolutions to achieve a linear travel of 1 inch. Using the number of revolutions turned on the bolt after it contacts the spring, the force can be computed by the equation:

$$F_{spring} = k_{spring} * (L_{free} - L) \quad 3-2$$

where F_{spring} is the force applied, k_{spring} is the spring constant, and $(L_{free} - L)$ is the change in the spring length.

3.5.1 Fixture Thermal Resistance Measurement

For the contact resistance measurements, it was necessary to provide a clamping force on the contact samples. This created an alternative heat path through the test fixture (referred to as the fixture path) that is unavoidable. Materials such as stainless steel and G10 were chosen for the fixture to increase the magnitude of the thermal resistance of this fixture path relative to the sample path resistance; however, the fixture path still allowed for an inherent parasitic heat leak. To account for all parasitic heat leaks when calculating the heat flux applied across the contact of interest, the fixture path thermal resistance measurement was taken. This was accomplished by cradling the top sample with a G10 support and hollow G10 rods and removing the bottom sample as shown in Figure 3-17. By removing the heat path through the bottom sample, the heat flux input by the heater was driven solely through the fixture path.



Figure 3-17. Fixture path measurement cradle and temperature sensor placement.

The temperature along two points of the fixture path, where T3 and T4 are mounted, were then measured for two given heat fluxes. Thermal resistance (in units K/W) was calculated using equation 3-3.

$$R = \frac{\Delta T}{Q} \quad 3-3$$

The measured fixture path resistance data can be seen in Figure 3-18, with the upper and lower errors in the x-axis temperature corresponding to the ΔT measured.

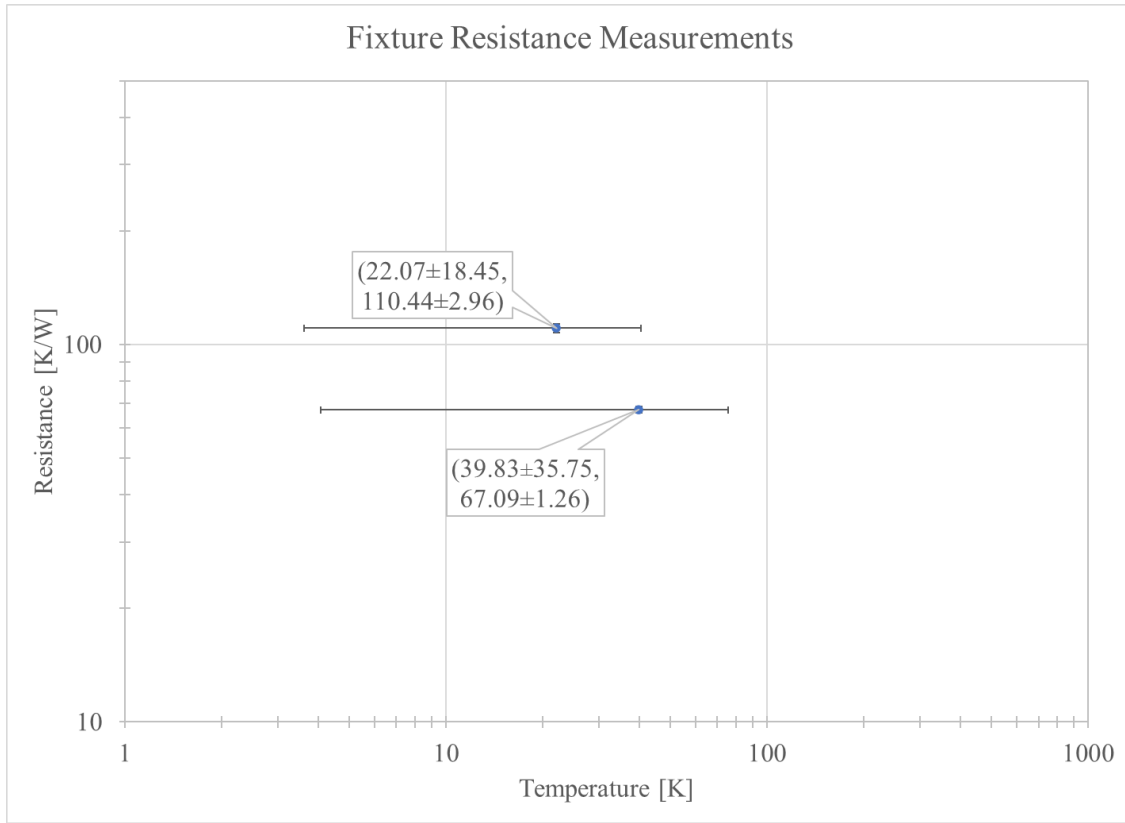


Figure 3-18. Fixture resistance measurements.

In order to predict the resistance in testing, an associated effective $\frac{L}{A}$ value was found for the fixture utilizing equation 3-4. This was done assuming the resistance corresponds to the temperature dependent conductivity of stainless steel, as most of the fixture structure is composed of stainless-steel.

$$R = \frac{L}{kA} = \frac{1}{k_{ss,intavg}} * \left(\frac{L}{A}\right)_{effective} \quad 3-4$$

Assuming a basic Fourier's law resistance, the $\frac{L}{A_{effective}}$ was found by utilizing the integrated average conductivity of stainless steel over the ΔT for each of the two resistance data points and backing out the $\frac{L}{A_{effective}}$ from the measured resistance as shown in the table of calculations, Table 3-1. From there, an average of the two $\frac{L}{A_{effective}}$ values was utilized for future measurements. Using these data, fixture heat leak was accounted for in the contact resistance calculations using the measured temperatures at the same two points and utilizing equation 3-4 to find the given fixture resistance corresponding to the test temperature, and then finally using equation 3-3 to find the $Q_{fixture}$, the parasitic heat leak in-test. In depth contact resistance calculations with these considerations are discussed further in Chapter 4.

Table 3-1. Calculations for fixture resistance accounting.

Bulk Conductivity Test Nominal Temperature Setting Matrix						
Data Point	Avg. T [K]	T3 [K]	T4 [K]	Int. Avg. k [W/m-K]	R [K/W]	L/A effective [1/m]
1	22.07	40.53	3.62	2.45	110.44	270.77
2	39.83	75.58	4.08	4.39	67.09	294.19
Average						282.48

3.6 Experimental Setup and Instrumentation

3.6.1 Instrumentation

The key instrumentation and equipment consisted of power supplies, a temperature monitor, and multimeters. A list of instrumentation including the models used, excluding heaters and temperature sensors, is provided in Table 3-2. In addition, a schematic of the instrumentation is shown in Figure 3-19.

Table 3-2. Instrumentation for experimental setup.

Instrumentation	Function
Granville-Phillips Micro Ion Plus Gauge	Vacuum chamber pressure readings.
Lake Shore 218 Temperature Monitor	Power and read all temperature sensors.
Keithley 2000 Multimeter	Measure main heater voltage.
HP 34401A Multimeter	Measure main heater current (shunt resistor voltage).
BK Precision 1698 DC Power Supply	Power to the main heater.
BK Precision 1687B DC Power Supply	Power to the trim heater.

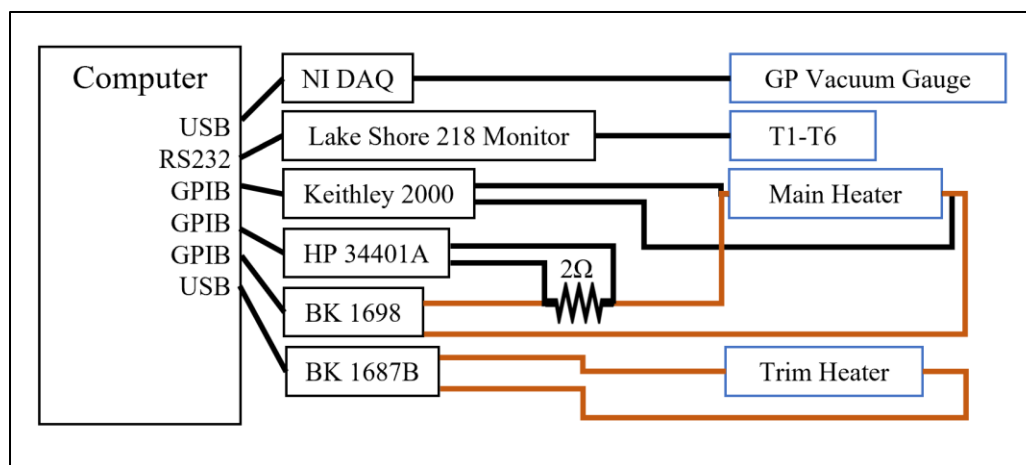


Figure 3-19. Instrumentation setup schematic.

LabView was utilized to control equipment as well as to collect data throughout all testing of bulk conductivity and contact resistance. The multimeters were used to record the main heater power through a four-wire measurement in order to correctly measure only the heater power and not the heat dissipated in the wires to and from the power supply and heater. The HP 34401A multimeter measured the main heater current through a voltage measurement across a high precision shunt resistor in series with the BK Precision 1698 DC power supply and the main heater. Both multimeters used for these measurements of power input received standard 1-year Z540.1 calibration before testing began.

3.6.2 Temperature Sensors and Heaters

Depending on the configuration, a different number of temperature sensors were mounted on the test fixture and stage for testing. For bulk conductivity measurements, two sensors were mounted on knife-edge clamps in the test fixture. For contact resistance measurements, four temperature sensors were mounted to clamps on the test fixture and two sensors were mounted to the test fixture itself to measure fixture heat leak. Two sensors that were always used for the test measurements were Cernox CX-1050-CU-HT-1.4L sensors, calibrated by Lake Shore Cryotronics over the temperature range of 1.40-325 Kelvin. The remaining sensors were germanium GR-200A-1000-4D sensors, which we calibrated against the Cernox sensors. All temperature sensors were powered by and read by the Lakeshore 218 Temperature Monitor in units of resistance (ohms) and these measurements were translated to temperature with calibration polynomial curves.

Two cartridge heaters were utilized in this test setup, one trim heater and one main test heater. The test heater is attached to a clamp and mounted to the top of each test fixture, as shown in all configurations previously, such as in Figure 3-15, and is utilized to apply the heat flux transfer rate to the sample for the resistance and conductivity measurements. The trim heater mounts directly to the second stage platform and acts to control the temperature of the cold head. The trim heater allows for the temperature of the overall testing to be shifted upwards, which is important in testing conductivity over a range of temperatures.

4 Methodology and Calculations

4.1 Bulk Conductivity Measurement and Calculation

The calculation of the bulk conductivity was rather simple. Reorganizing Fourier's Law, shown in equation 4-1, the conductivity of a material can be expressed as a function of the temperature difference across a given cross section and length for a given heat flux, as shown in equation 4-2.

$$Q_{sample} = kA_c * \frac{\Delta T_{measured}}{L_{sensors}} \quad 4-1$$

$$k = \frac{Q_{sample}}{\Delta T_{measured}} * \frac{L_{sensors}}{A_c} \quad 4-2$$

Once a sample was mounted in place, measurements of the length between the knife edge sensors and the diameter of the copper rods to ascertain the cross-sectional area were taken with calipers five times each and recorded. The averages of these measurements were utilized to calculate the conductivity and the associated standard deviation of the five measurements was used in the calculation of the random uncertainty of the measurement, further described in Chapter 5.1.

For the heater and temperature measurements, an intrinsic parasitic heat flux was present that created an inherent temperature differential between the sensors even when there was no heater input; this parasitic heat flux varied for each sample. In order to account for and remove this parasitic temperature differential from our calculations, the trim heater was increased in set increments and the inherent temperature differential across an array of average temperatures was recorded. The parasitic dT follows a power law relation with the average temperature, and for the conductivity recorded readings the associated power law for a given sample would be used to extrapolate to zero power and this zero power or inherent temperature differential was subtracted from the total read temperature differential.

For the conductivity measurements themselves, the heaters were adjusted to ensure a minimum temperature differential required to achieve a certain uncertainty within the final conductivity measurement. The larger the driven temperature differential, the lower the conductivity measurement uncertainty; however, a larger driven temperature differential also resulted in a larger uncertainty in the

‘average’ temperature associated with the reading. A table of the test protocol used for minimum dT for a given set of allowable uncertainties (5% to 15%) are shown below in Table 4-1. For each measurement, the system was allowed to reach a steady state and 200 data points were recorded and averaged for the temperature and heater measurements. In order to capture the shape of the conductivity curve, 10-12 measurements were taken nominally following a logarithmic scale between 4 K and 40 K.

Table 4-1. Nominal setpoints and corresponding minimum dT values.

Bulk Conductivity Test Nominal Temperature Setting Matrix					
dk/k = 5%		dk/k = 10%		dk/k = 15%	
Average T	Minimum dT	Average T	Minimum dT	Average T	Minimum dT
4.5	0.1814	4.5	0.08871	4.5	0.05888
5	0.1929	5	0.09435	5	0.06263
5.5	0.2066	5.5	0.101	5.5	0.06707
6	0.2222	6	0.1087	6	0.07214
6.5	0.2395	6.5	0.1172	6.5	0.07779
7	0.2585	7	0.1265	7	0.08396
8	0.3006	8	0.1471	8	0.09769
9	0.3478	9	0.1702	9	0.113
10	0.3994	10	0.1955	10	0.1298
12	0.514	12	0.2517	12	0.1671
15	0.712	15	0.3487	15	0.2316
20	1.105	20	0.5412	20	0.3594
30	2.117	30	1.037	30	0.6883
40	3.428	40	1.676	40	1.113

4.2 Contact Resistance

For the contact resistance measurements, a similar testing methodology was utilized. First, the main parasitic measurements were taken to account for inherent parasitic temperature differences within the measured temperature differentials. For each test, this consisted of again increasing the trim heater in set increments while maintaining no heat input in the main heater to find a power law relation for the parasitic temperature differentials for a given average temperature. For this test fixture, because it has low thermal diffusivity elements such as stainless steel in the fixture it was necessary to allow longer periods of stabilization before recording steady state data.

After this parasitic test, the main test consisted of setting the main heater to a set heat input and then varying the trim/main heater input to adjust the average temperature. For the dry testing, the trim heater could be used for all average temperature adjustments. But due to the very low resistance of the TIM contacts it was necessary to utilize the main heater in order to drive larger temperature differentials and ensure uncertainty remained as relatively low as possible. The testing for dry measurements was run for 12 test points from the lowest achievable temperature around 4 K to 20 K on a nominal log scale. For TIM measurements, the same 12 test points were run but on a scale from the lowest achievable to 10 K; due to the low resistance of the TIM contact resistance, the uncertainties at higher temperatures became unreasonable for the data. Again, due to the nature of the test fixture longer periods of stabilization before steady state data are recorded are required in comparison to bulk conductivity testing.

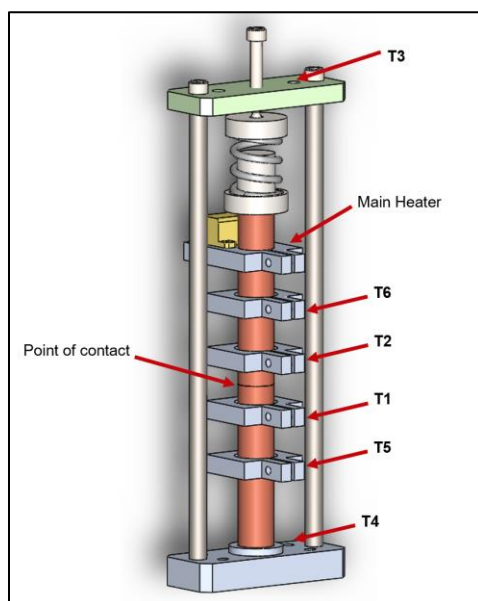


Figure 4-1. Contact fixture with temperature sensor placement.

The calculation of the contact resistance was performed with accounts for fixture heat leak as well as the bulk material resistance between where the sensors were located and the actual contact itself. The numbered sensors are placed as seen in Figure 4-1 and the sensors are referred to with these numbers in the subsequent calculations. The basis of the contact resistance calculation, as described in Chapter 1.3, is the temperature differential across the contact divided by the heat flux multiplied by the apparent contact

area, given by equation 1-2. The elements of this equation are calculated separately with calculations accounting for bulk resistance contributions to the temperature differential and fixture heat leak reducing the heat flux, and then combined.

The temperature differential of interest across the contact can be estimated using T2-T1 for situations where the bulk resistance contribution to the ΔT is orders of magnitudes smaller than the contact resistance. However, in cases of very low contact resistance the bulk conductivity can play a role in measurement and therefore should be accounted for. Although we did measure T5 and T6 to assemble a temperature profile, the temperature gradient was too small for the testing carried out here to establish the bulk resistance with any precision because the differentials were often within the uncertainty of the sensors due to their very close positioning and the high conductivity of the C101 copper. Instead, bulk conductivity data collected for the samples in the bulk conductivity section of testing prior to contact testing was utilized to calculate the temperature drop in the length between the T1 and T2 sensors for the bulk material.

The main resistance calculation is given by equation 4-3 where R is the area-specific resistance in units $\left[\frac{m^2-K}{W}\right]$, T_1 and T_2 are the notated temperatures, A_c is the apparent contact area in $[m^2]$, ΔT_{Bulk} is the calculated bulk material dT between the sensors and the contact, and Q is the heat flux across the contact. Shown in equation 4-4, ΔT_{Bulk} is calculated using Fourier's Law. The lengths between the sensors and the contact, L_1 and L_2 , are measured and recorded, and multiplied by the heat flux, and divided by the contact area and the integrated average C101 bulk conductivity between the sensor temperatures. The k_{C101} integrated average value is calculated as a function of T_1 and T_2 . The heat flux value is calculated from the four-wire measurement of the voltage and current applied across the main heater and the fixture parasitic heat loss, given in equation 4-5. The V_K value is the voltage in $[W]$ measured across the heater and V_{HP} $[W]$ is the voltage measured across the shunt resistor, $R_{shunt} = 2 [\Omega]$, which is in line with the main heater power supply. The second portion of equation accounts for the

fixture heat loss, manipulated from equation 3-3. The heat lost to the fixture is equal to the measured temperature differential on the two fixture sensors, T_3 and T_4 , divided by the given fixture resistance. Like the k_{C101} value, $R_{fixture}$ is a function of T_3 and T_4 .

$$R = \frac{T_2 - T_1 - \Delta T_{Bulk}}{Q} * A_c \quad 4-3$$

$$\Delta T_{Bulk} = \frac{Q * (L_1 + L_2)}{k_{C101} * A_c} \quad 4-4$$

$$Q = V_K * \frac{V_{HP}}{R_{shunt}} - \frac{T_3 - T_4}{R_{fixture}} \quad 4-5$$

All of these calculations, including the functions that calculate given k_{C101} and $R_{fixture}$ values, in addition to the uncertainty calculations, were carried out using a MATLAB program written for this contact resistance data processing.

4.2.1 Surface Imaging and Pressure Application Measurement Methodology

Before every contact resistance test, the surfaces were imaged with an Alicona InfiniteFocus G4. This device utilizes focus variation to map and record the surface. From these data, measurements of roughness and flatness were recorded before each test in addition to the 2D area scan imaging. An example of an imaged surface can be seen in Figure 4-2.

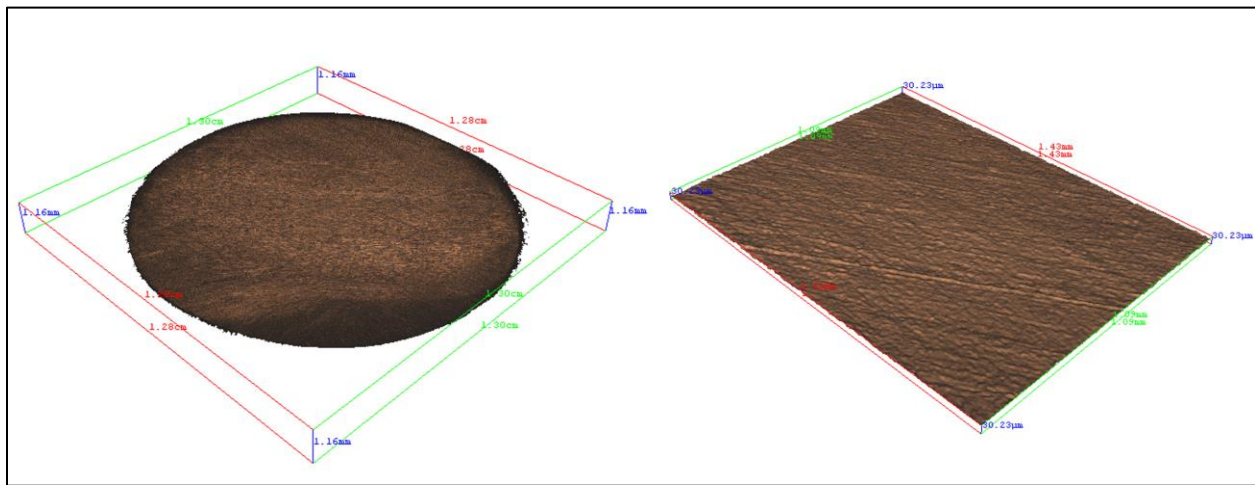


Figure 4-2. Alicona surface imaging example.

While placing the samples in the fixture, Super Low Fujifilm Prescale Pressure Paper, which can record a range of pressure from 0.5-2.5 MPa, was pressed between the samples under the same spring force utilized for the test [17]. This pressure sensitive film allows us to characterize the uniformity and distribution of the applied pressure for the contacts.

4.3 Force Calculations for Contact Pressure Application

The nominal calculation for applying force is found through Hooke's Law, given in equation 4-6 where k_{spring} is the spring constant, F_{spring} is the force applied by the compressed spring, and $(L_{free} - L)$ is the length of compression of the spring in the axial direction. We can then get the relation to find the correct force for our given rods using the pressure-force relation in equation 4-7 where P is pressure, F is force and A_c is cross-sectional. The copper rods have a nominal diameter of 0.5 inches and a nominal cross-sectional area equivalent to 0.196 in² or 1.27 cm². The desired nominal 'low' and 'high' pressures were chosen to match closely with previous NGC data, which were carried out at pressures of 0.27 and 1.97 MPa (equivalently 39.2 lbf/in² and 286 lbf/in²) [10]. As previously mentioned, the spring is compressed with an #8-32 bolt for which 32 turns of the bolt is equivalent to one inch traveled or one inch of compression on the spring.

$$F_{spring} = k_{spring} * (L_{free} - L) \quad 4-6$$

$$P = \frac{F}{A_c} \quad 4-7$$

The spring that was utilized has a spring constant of 165 lb_f/in and a free length of 1 inch. To match the given pressures, the calculated lengths of compression, $(L_{free} - L)$, would be 0.048 inches and 0.34 inches, which correspond to 1.5 and 11 turns of the #8-32 bolt, respectively. These guidelines were utilized to turn the bolt and apply the nominal correct force for each test. For the 'high' pressure tests though, 11 turns correspond to slightly over the fully compressed length of the spring, so it was instead tightened to full compression. For the spring that was utilized the fully compressed maximum load was 55

pounds, so for the surface area of the rods, this translates to a pressure of 280 lbf/in² or 1.93 MPa, slightly deviating from the NGC ‘high’ pressure of 286 lbf/in².

5 Results and Discussion

For bulk conductivity testing, five samples of C101 and C110 each were tested and compared. These samples were purchased from Sequoia Brass & Copper and cut from single ½-inch diameter rods of material. For contact resistance, a selection of the bulk conductivity samples were cut into smaller samples and the test matrix provided in Table 5-1 was completed. The main point of interest for contact measurements was variability and repeatability in resistance for a set contacts made several different times and multiple sets of contacts made with the same pressure and TIM material, as well as tracking and documenting surface roughness.

Table 5-1. Test matrix.

<i>Test Type</i>	<i>No. of Specimens</i>	<i>Tests per Specimen</i>	<i>Bulk Material</i>	<i>Dry/TIM</i>	<i>Roughness</i>	<i>Pressure</i>	<i>Total Tests</i>
<i>Bulk</i>	5	1	C110	N/A	N/A	N/A	5
<i>Bulk</i>	5	1	C101	N/A	N/A	N/A	5
<i>Contact</i>	2	3	C101	Dry	As recorded*	High	6
<i>Contact</i>	2	3	C101	Apiezon Grease	As recorded*	High	6
<i>Contact</i>	2	3	C101	Indium Foil	As recorded*	High	6

* Polished surfaces in the range of 1 micron RMS surface roughness.

5.1 Uncertainty Analysis

5.1.1 Temperature Sensor Uncertainty

The uncertainty of the temperature sensors read with the 218 Lakeshore Temperature Monitor includes the calibration curve uncertainty, and the measurement resolution and the electronic uncertainty of the temperature monitor. The equations for the total uncertainty, bias uncertainty and random uncertainty are listed below in equations 5-1, 5-2, and 5-3, respectively.

$$U_T = \sqrt{(B_T)^2 + (P_T)^2} \quad 5-1$$

$$B_T = \sqrt{(B_{218m})^2 + (B_{218e})^2 + (B_{calib})^2} \quad 5-2$$

$$P_T = 2 * STDEV_T \quad 5-3$$

The random uncertainty, P_T , was ascertained by measuring 200 data points and averaging them and utilizing the associated standard deviation. The 218 monitor's electronic accuracy and measurement resolution for negative temperature coefficient RTDs are listed below in resistance units in equations 5-4 and 5-5 respectively [18].

$$B_{218m} = 0.050 [\Omega] \quad 5-4$$

$$B_{218e} = 0.8 [\Omega] + 0.04\% RDG \quad 5-5$$

The symbol *RDG* denotes the resistance reading of a given sensor in ohms. For the Cernox and germanium sensors utilized, these resistance equations can be expressed in temperature units utilizing the R-T relations of each sensor. For our Cernox sensors, T1 and T2, the bias equations in temperature units are given below in equations 5-6, 5-7, and 5-8 where T indicates the recorded temperature measurement.

$$B_{218m,cernox} = (7E - 6) * T^2 - 0.0003 * T + 0.0022 \quad 5-6$$

$$B_{218e,cernox} = (5E - 5) * T^2 + 0.001 * T - 0.0029 \quad 5-7$$

$$B_{calib,cernox} = (1E - 9) * T^3 - (4E - 7) * T^2 + 0.0002 * T + 0.0037 \quad 5-8$$

For the germanium sensors, because they were calibrated using the Cernox sensors there is additional uncertainty propagated in their calibration from our Cernox curves, propagated in equation 5-11. Each of the germanium sensors also had a unique R-T relation for the measurement and electronic uncertainties, as indicated by the coefficients A , B , and C in equations 5-9 and 5-10. The associated coefficients for the germanium sensors, T3-T6, are given in

Table 5-2.

$$B_{218m,germ} = A * T^B \quad 5-9$$

$$B_{218e,germ} = C * T^B + 0.0004 * T \quad 5-10$$

$$B_{calib,germ} = \sqrt{(B_{218m,cernox})^2 + (B_{218e,cernox})^2 + (B_{calib,cernox})^2} \quad 5-11$$

Table 5-2. Germanium sensor coefficients for uncertainty equations.

Germanium Sensor Uncertainty Equations Coefficients			
Sensor	A	B	C
T3	6E-6	2.8086	9E-5
T4	3E-6	2.9448	4E-5
T5	6E-6	2.9982	4E-5
T6	2E-6	2.9849	4E-5

5.1.2 Applied Heat Uncertainty

5.1.2.1 Bulk Conductivity Applied Heat Uncertainty

The heat flux applied across the bulk sample is measured through a 4-wire measurement, with two multimeters reading voltages across the heater itself and a high precision shunt resistor, given by the equation 5-12. The total uncertainty as well as the bias and random uncertainty equations are given as equations 5-13, 5-14, and 5-15 respectively. The random uncertainty is calculated using the same method as temperature readings, utilizing the standard deviation of 200 data points.

$$Q = V * I = V_K * \left(\frac{V_{HP}}{R_{shunt}} \right) [W] \quad 5-12$$

$$U_Q = \sqrt{(B_Q)^2 + (P_Q)^2} \quad 5-13$$

$$B_Q = \sqrt{(B_{para})^2 + (B_{Q,meas})^2} \quad 5-14$$

$$P_Q = 2 * STDEV_Q \quad 5-15$$

The parasitic uncertainty in the heater measurement, B_{para} , is the conservative maximum radiation heat leak calculated for a sample with an assumed surface emissivity of 1 radiating from 10 K to the stage at 3.5 K and is equal to $3.409E - 4 [W]$. The stage temperature is never this far from the sample temperature itself and tracks with it, so this conservative estimate at the lowest available stage temperature is used to characterize this heat leak.

For the measurement uncertainty, $B_{Q,meas}$, the uncertainty from the calibrated multimeters and the uncertainty in the precision of the shunt resistor are propagated through equation 5-16. The derivations for the partial derivatives in this propagation are given in equations 5-17, 5-18, and 5-19. In these equations, Q is the applied heat, V_K is the voltage measured across the heater, V_{HP} is the voltage measured across the shunt resistor, and R_{shunt} is the shunt resistor's resistance of 2 ohms.

$$B_{Q,meas} = \sqrt{\left(\frac{\partial Q}{\partial V_K} B_{V_K}\right)^2 + \left(\frac{\partial Q}{\partial V_{HP}} B_{V_{HP}}\right)^2 + \left(\frac{\partial Q}{\partial R_{shunt}} B_{R_{shunt}}\right)^2} \quad 5-16$$

$$\frac{\partial Q}{\partial V_K} = \frac{V_{HP}}{R_{shunt}} = \frac{V_{HP}}{2\Omega} \quad 5-17$$

$$\frac{\partial Q}{\partial V_{HP}} = \frac{V_K}{R_{shunt}} = \frac{V_K}{2\Omega} \quad 5-18$$

$$\frac{\partial Q}{\partial R_{shunt}} = -V_K * \frac{V_{HP}}{(R_{shunt})^2} = -\frac{V_K * V_{HP}}{(2\Omega)^2} \quad 5-19$$

The calibrated Keithley 2000 multimeter and HP34401A multimeter have associated uncertainties given by equations 5-20 and 5-21 respectively. The 2-ohm shunt resistor has a 0.02% associated uncertainty, $B_{R_{shunt}} = 0.0004 [\Omega]$. Combining these uncertainties with the partial derivations to propagate the uncertainty, the total measured uncertainty is given by equation 5-22.

$$B_{V_K} = 0.003 * V_K + 0.005 [V] \quad 5-20$$

$$B_{V_{HP}} = 4E - 5 * V_{HP} + 7E - 6 [V] \quad 5-21$$

$$B_{Q,meas} = \sqrt{\left(\frac{V_{HP}}{2} (.003 * V_K + .005)\right)^2 + \left(\frac{V_K}{2} (4E - 5 * V_{HP} + 7E - 6)\right)^2 + (.0001 * V_K * V_{HP})^2} \quad 5-22$$

5.1.2.2 Contact Resistance Applied Heat Uncertainty

When calculating the applied heat for contact resistance, as described in Chapter 4.2, we additionally account for the fixture heat leak. In this case, the equation is slightly altered from the bulk measurement and the calculation and uncertainty relations are given below in equations 5-23, 5-24, 5-25, and 5-26.

$$Q = V_K * \frac{V_{HP}}{R_{shunt}} - Q_{fixture} = V_K * \frac{V_{HP}}{R_{shunt}} - \frac{T_3 - T_4}{R_{fixture}} \quad 5-23$$

$$U_Q = \sqrt{(B_Q)^2 + (P_Q)^2} \quad 5-24$$

$$B_Q = \sqrt{(B_{para})^2 + (B_{Q,meas})^2 + (B_{Q,fixture})^2} \quad 5-25$$

$$P_Q = 2 * STDEV_Q \quad 5-26$$

The calculations for B_{para} and $B_{Q,meas}$ are the same as those utilized in the bulk conductivity applied heater uncertainty, given by $B_{para} = 3.409E - 4 [W]$ and the equation 5-22 respectively. For the fixture heat leak, the uncertainty of the temperature sensors and the fixture resistance are propagated in equation 5-27 where the temperature uncertainties are calculated with the given relations in Chapter 5.1.1 and fixture resistance uncertainty is propagated from the calculation of the resistance given in Chapter 3.5.1, and handled through MATLAB.

$$B_{Q,fixture} = \sqrt{\left(\frac{B_{T3}}{R_{fixture}}\right)^2 + \left(\frac{B_{T4}}{R_{fixture}}\right)^2 + \left(\frac{T_4 - T_3}{R_{fixture}} B_{R_{fixture}}\right)^2} \quad 5-27$$

5.1.3 Length and Cross-Sectional Area Measurement Uncertainty

The length between knife-edge sensors and the diameters of the rods were both measured with calipers and averaged from five measurements for each test. For the length and diameter measurements, the resolution bias uncertainty of the calipers was 0.00001 m. This diameter measurement bias uncertainty was propagated to a cross-sectional measurement as shown from the relation in equations 5-28 and 5-29. The random uncertainty for measurements were determined from the standard deviation, shown in equation 5-30, and the total uncertainty of the area is given in equation 5-31.

$$A = \frac{\pi D^2}{4} \quad 5-28$$

$$B_A = \sqrt{\left(\frac{\partial A}{\partial D} * 0.00001 [m]\right)^2} = \sqrt{\left(\frac{\pi D * 0.00001}{2}\right)^2} \quad 5-29$$

$$P_A = 2.5706 * STDEV_A \quad 5-30$$

$$U_A = \sqrt{B_A^2 + P_A^2} \quad 5-31$$

The values and relations for the total and bias and random uncertainty of the length measurements are shown in equations 5-32, 5-33, and 5-34.

$$B_L = 0.00001 [m] \quad 5-32$$

$$P_L = 2.5706 * STDEV_L \quad 5-33$$

$$U_L = \sqrt{B_L^2 + P_L^2} \quad 5-34$$

5.1.4 Bulk Conductivity Total Uncertainty

The bulk conductivity is calculated with the equation 5-35 and has a total uncertainty given in equation 5-36. The propagated bias and random uncertainty from the measurement of the variables is given by equations 5-37 and 5-38.

$$k = \frac{Q * L}{A * (T_1 - T_2)} \quad 5-35$$

$$U_k = \sqrt{(B_k)^2 + (P_k)^2} \quad 5-36$$

$$B_k = \sqrt{\left(\frac{\partial k}{\partial Q} B_Q\right)^2 + \left(\frac{\partial k}{\partial L} B_L\right)^2 + \left(\frac{\partial k}{\partial A} B_A\right)^2 + \left(\frac{\partial k}{\partial T_1} B_{T1}\right)^2 + \left(\frac{\partial k}{\partial T_2} B_{T2}\right)^2} \quad 5-37$$

$$P_k = \sqrt{\left(\frac{\partial k}{\partial Q} P_Q\right)^2 + \left(\frac{\partial k}{\partial L} P_L\right)^2 + \left(\frac{\partial k}{\partial A} P_A\right)^2 + \left(\frac{\partial k}{\partial T_1} P_{T1}\right)^2 + \left(\frac{\partial k}{\partial T_2} P_{T2}\right)^2} \quad 5-38$$

These partial derivations are solved in the equations 5-39 through 5-43 below. Again, all of the bulk uncertainty is calculated with the data processed within MATLAB.

$$\frac{\partial k}{\partial Q} = \frac{L}{A * (T_1 - T_2)} \quad 5-39$$

$$\frac{\partial k}{\partial L} = \frac{Q}{A * (T_1 - T_2)} \quad 5-40$$

$$\frac{\partial k}{\partial A} = -\frac{Q * L}{A^2 * (T_1 - T_2)} \quad 5-41$$

$$\frac{\partial k}{\partial T_1} = -\frac{Q * L}{A * (T_1 - T_2)^2} \quad 5-42$$

$$\frac{\partial k}{\partial T_2} = \frac{Q * L}{A * (T_1 - T_2)^2} \quad 5-43$$

5.1.5 Contact Resistance Total Uncertainty

The uncertainty of the contact resistance measurement, calculated in equation 5-44, is given by the equations 5-45, 5-46, and 5-47, which are the total, bias, and random uncertainties, respectively.

$$R = \frac{T_2 - T_1 - \Delta T_{Bulk}}{Q} * A_c \quad 5-44$$

$$U_R = \sqrt{(B_R)^2 + (P_R)^2} \quad 5-45$$

$$B_R = \sqrt{\left(\frac{\partial R}{\partial Q} B_Q\right)^2 + \left(\frac{\partial R}{\partial \Delta T_{Bulk}} B_{\Delta T_{Bulk}}\right)^2 + \left(\frac{\partial R}{\partial T_1} B_{T1}\right)^2 + \left(\frac{\partial R}{\partial T_2} B_{T2}\right)^2 + \left(\frac{\partial R}{\partial A_c} B_{Ac}\right)^2} \quad 5-46$$

$$P_R = \sqrt{\left(\frac{\partial R}{\partial Q} P_Q\right)^2 + \left(\frac{\partial R}{\partial \Delta T_{Bulk}} P_{\Delta T_{Bulk}}\right)^2 + \left(\frac{\partial R}{\partial T_1} P_{T1}\right)^2 + \left(\frac{\partial R}{\partial T_2} P_{T2}\right)^2 + \left(\frac{\partial R}{\partial A_c} P_{Ac}\right)^2} \quad 5-47$$

The partial derivatives for these relations are given below in equations 5-48 through 5-52.

$$\frac{\partial R}{\partial Q} = -\frac{T_2 - T_1 - \Delta T_{Bulk}}{Q^2} * A_c \quad 5-48$$

$$\frac{\partial R}{\partial \Delta T_{Bulk}} = -\frac{A_c}{Q} \quad 5-49$$

$$\frac{\partial R}{\partial T_1} = -\frac{A_c}{Q} \quad 5-50$$

$$\frac{\partial R}{\partial T_2} = \frac{A_c}{Q} \quad 5-51$$

$$\frac{\partial R}{\partial A_c} = \frac{T_2 - T_1 - \Delta T_{Bulk}}{Q} \quad 5-52$$

For the ΔT_{Bulk} value, more uncertainty is propagated from its calculation, shown in equation 5-53.

The bias and random uncertainty are given in equations 5-54 and 5-55 and the derivations for the $B_{\Delta T_{Bulk}}$ are given in equations 5-56 through 5-60. The k_{C101} value and its associated uncertainty are calculated within the MATLAB program and

$$\Delta T_{Bulk} = \frac{Q * (L_1 + L_2)}{k_{C101} * A_c} \quad 5-53$$

$$B_{\Delta T_{Bulk}} = \sqrt{\left(\frac{\partial \Delta T_{Bulk}}{\partial Q} B_Q\right)^2 + \left(\frac{\partial \Delta T_{Bulk}}{\partial A_c} B_{A_c}\right)^2 + \left(\frac{\partial \Delta T_{Bulk}}{\partial L_1} B_{L1}\right)^2 + \left(\frac{\partial \Delta T_{Bulk}}{\partial L_2} B_{L2}\right)^2 + \left(\frac{\partial \Delta T_{Bulk}}{\partial k_{C101}} B_{k_{C101}}\right)^2} \quad 5-54$$

$$P_{\Delta T_{Bulk}} = 2 * STDEV_{\Delta T_{Bulk}} \quad 5-55$$

$$\frac{\partial \Delta T_{Bulk}}{\partial Q} = \frac{(L_1 + L_2)}{k_{C101} * A} \quad 5-56$$

$$\frac{\partial \Delta T_{Bulk}}{\partial A_c} = -\frac{Q * (L_1 + L_2)}{k_{C101} * A_c^2} \quad 5-57$$

$$\frac{\partial \Delta T_{Bulk}}{\partial L_1} = \frac{Q}{k_{C101} * A_c} \quad 5-58$$

$$\frac{\partial \Delta T_{Bulk}}{\partial L_2} = \frac{Q}{k_{C101} * A_c} \quad 5-59$$

$$\frac{\partial \Delta T_{Bulk}}{\partial k_{C101}} = -\frac{Q * (L_1 + L_2)}{k_{C101}^2 * A} \quad 5-60$$

5.2 Bulk Conductivity Results

The bulk conductivity of 10 samples were tested according to the given protocol. Five C101 and five C110 samples were each cut from 0.5-inch diameter rods. Each sample was 6 inches long and cut from the same rod stock for each material (C101 and C110) respectively. These rods were purchased from Sequoia Brass & Copper [19]. The results for C110 and C101 can be seen below in Figure 5-1 and Figure 5-2 respectively. In these results, it can be seen that the C101 rods all have very consistent bulk conductivities. The C110 sample 5 did have a slightly higher conductivity curve than the other four samples. This was confirmed through multiple tests and while it is uncertain the cause, this variation could possibly have been a product of a difference in this particular sample's work hardening from machining when cutting the rods. While this process was seemingly consistent, a possibility is that perhaps this piece was an end of the rod that received less machining, one cut instead of two, which allowed it to maintain a higher conductivity.

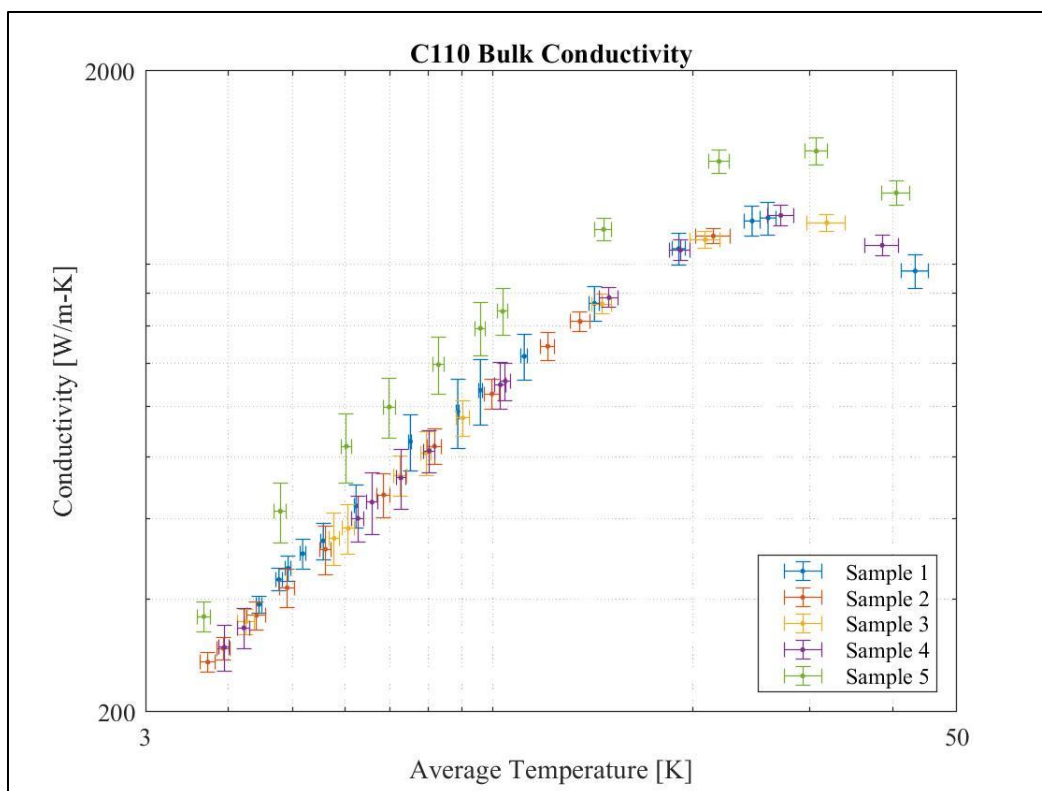


Figure 5-1. Sequoia Brass & Copper C110 Bulk Conductivity Results

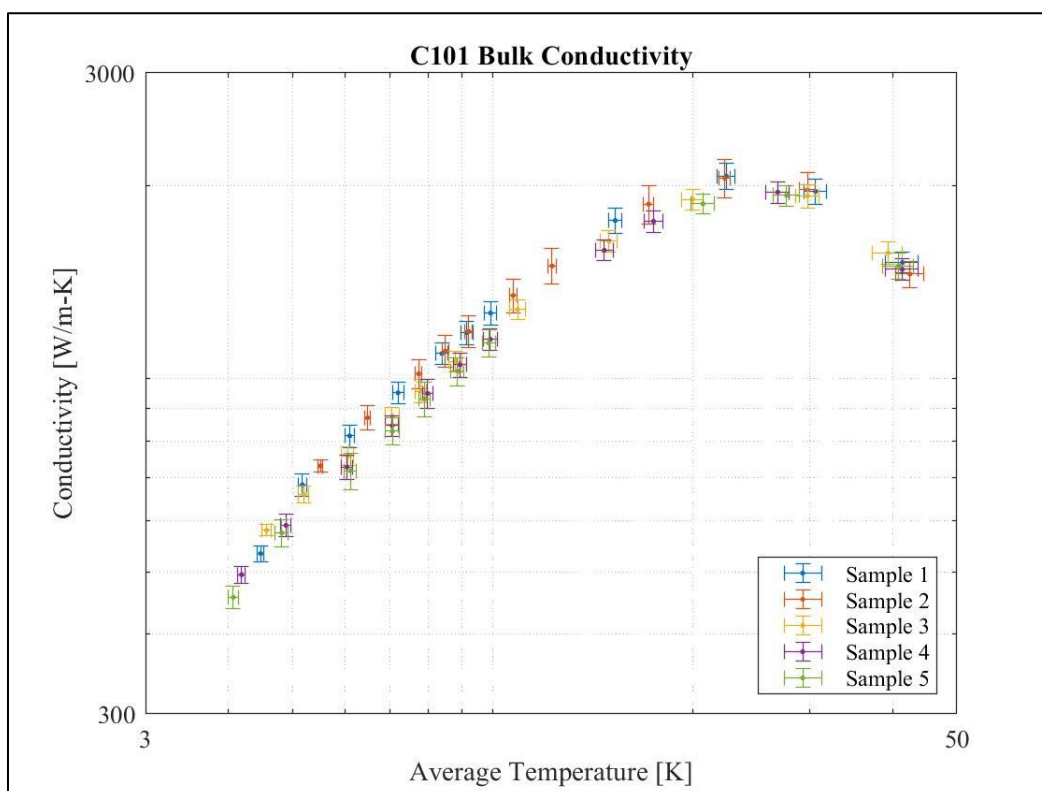


Figure 5-2. Sequoia Brass & Copper C101 Bulk Conductivity Results.

5.2.1 Comparison with Literature and Expected RRR

C101 copper rods have an associated oxygen-free purity of 99.99% [19]. For this purity level, the expected RRR range is typically 100-500, although it can vary greatly [20]. In our testing, we can compare the bulk conductivity of our measured C101 samples with the known conductivity curves for given RRR values, available through NIST [15]. This comparison is shown graphically in Figure 5-3. As can be seen, the conductivity of the C101 samples was substantially lower than would be assumed based on an RRR of 100-500. The material performed more in line with an RRR of 70-80. This is an example of why it is important to note that assumptions of these thermal characteristics for certain copper at cryogenic temperatures should be carefully assessed to accurately model thermal systems. Assuming a RRR in the range of 100-500 would yield very different expected thermal conductivity behavior than would be truly exhibited in-situ with this material.

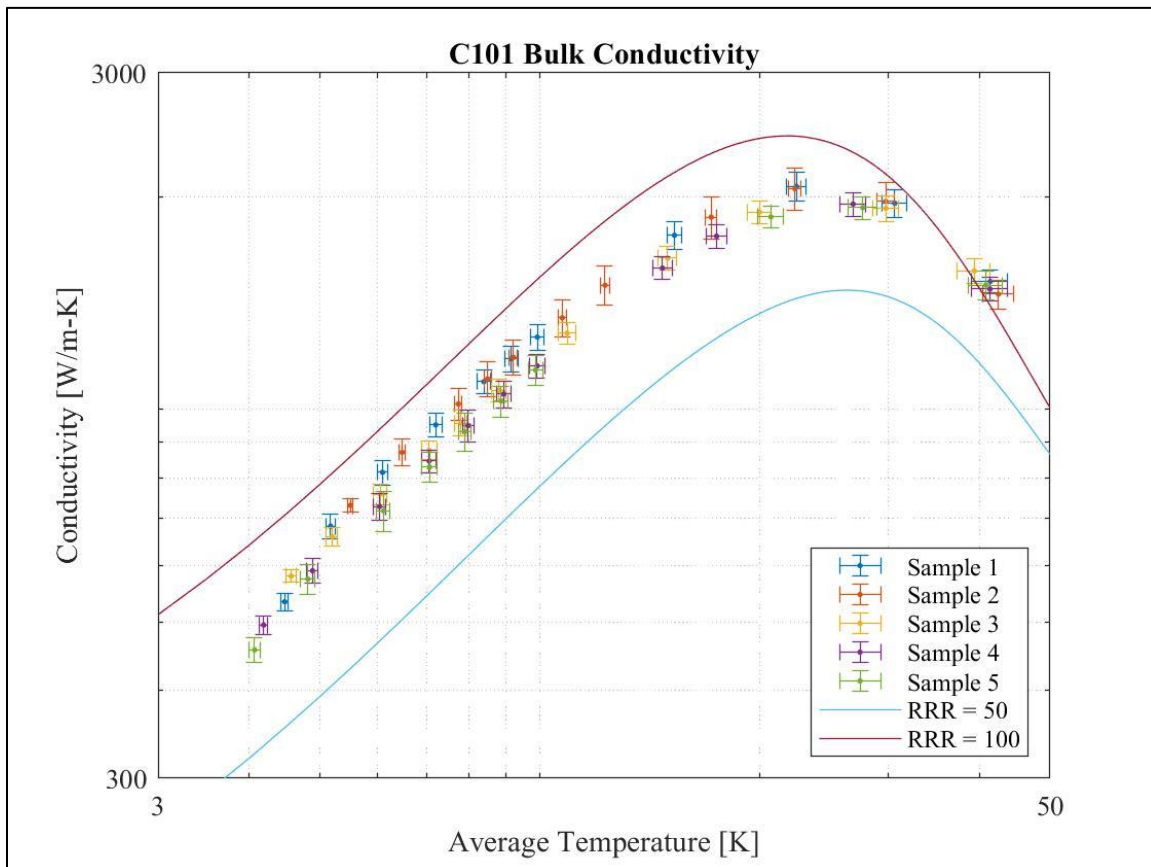


Figure 5-3. Comparison of C01 bulk conductivity with known RRR curves.

5.3 Contact Resistance Results

The key contact measurements can be found in Figure 5-4, Figure 5-5 and Figure 5-6 corresponding to three kinds of contacts: dry contacts, contacts with a 5 mm indium foil TIM, and contacts mated with Apiezon grease. All of these contacts were assembled under high pressure for two sample sets, and each sample set was de-mated and mated twice for a total of three measurements each. This allowed us to observe the variation within each sample set that occurs when it is mated multiple times, as well as the variation between two sample sets that are fabricated from the same lot of bulk material. We saw the lowest contact resistance in the indium contacts and, as expected, the highest resistance in the dry Cu-Cu contacts.

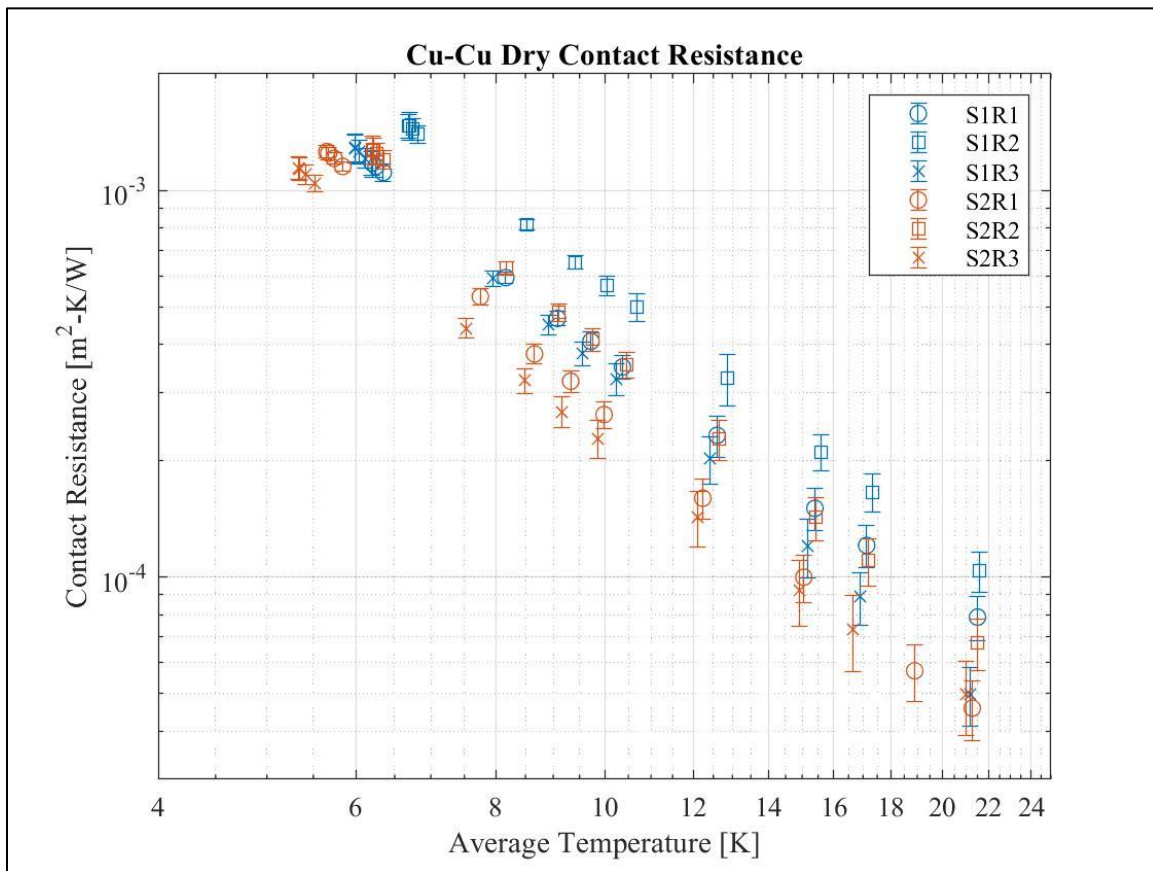


Figure 5-4. Dry contact Cu-Cu thermal resistance data.

For the dry data, it can be seen that there was a good deal of variation in the contact resistance among the contacts. The variation in contact resistance did not follow an obvious pattern in terms of increasing or decreasing with the progression of de-mating and mating cycles. For each sample's dry data, a power law

was fit to each of the three datasets and the associated resistance for each run's curve fit for a temperature of 6 K was found and these values were then averaged. For sample 1, the average resistance at 6 K was $1.45E - 3 \left[\frac{m^2K}{W} \right] \pm (15.5\%, 27.9\%)$. The values from the individual curve fits varied by a maximum percent deviation of 15.5% below and 27.9% above the average resistance value, notated as $\pm(15.5\%, 27.9\%)$. For sample 2, the average value and maximum deviations of the individual runs was $1.07E - 3 \left[\frac{m^2K}{W} \right] \pm (24.2\%, 27.0\%)$.

For the indium contacts, sample 1's data yielded an average resistance and deviation of $6.13E - 5 \left[\frac{m^2K}{W} \right] \pm (17.7\%, 10.6\%)$, and sample 2's data yielded an average resistance of $7.94E - 5 \left[\frac{m^2K}{W} \right] \pm (14.7\%, 16.8\%)$.

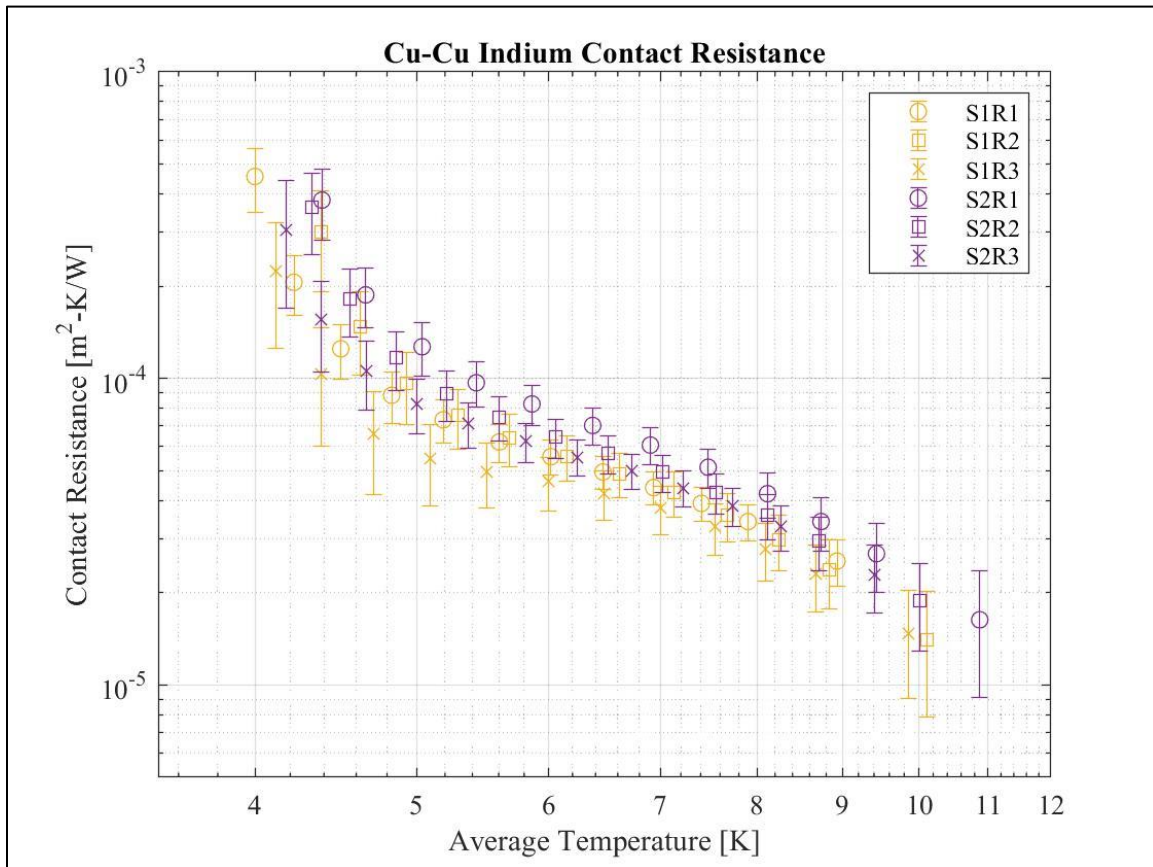


Figure 5-5. Indium foil Cu-Cu contact thermal resistance data.

The grease TIM contact resistance sample 1 data gave an average resistance and deviation of $9.94E - 5 \left[\frac{m^2 K}{W} \right] \pm (5.9\%, 11.0\%)$ and sample 2 yielded $9.28E - 5 \left[\frac{m^2 K}{W} \right] \pm (10.3\%, 9.9\%)$. From this variation, we can see that although indium yields the lowest resistance, the grease data had lower deviations in the results for the contacts that were made and re-made. These percentages in variation show quantitatively that dry contacts vary the greatest in their resistance when assembled multiple times in the same conditions, while grease contacts were comparatively reliable in repeatability of the measured resistance.

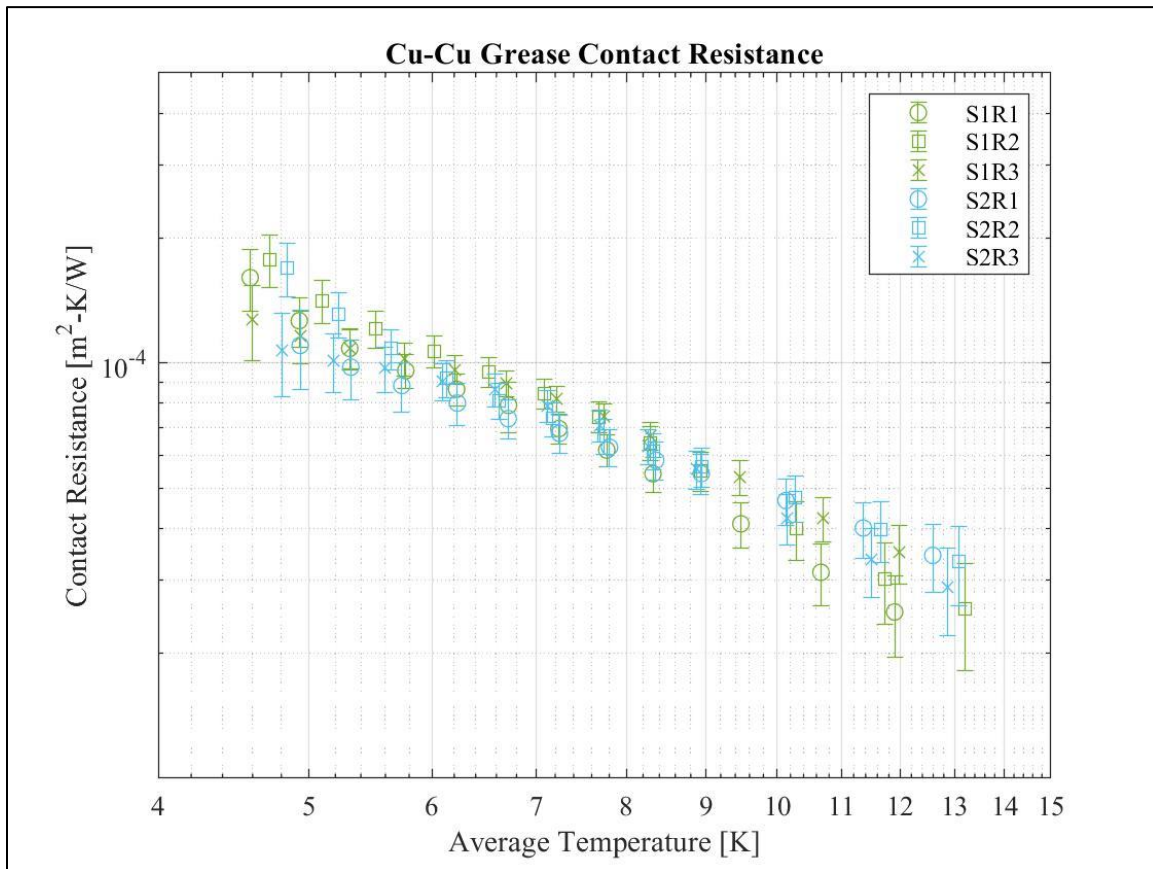


Figure 5-6. Apiezon-N grease Cu-Cu contact thermal resistance data.

5.3.1 Surface Imaging

In addition to the contact resistance data itself, surface measurements were taken before each test. The data for the flatness of the images was obtained using 5x resolution on the Alicona G4 InfiniteFocus and imaged over the entire surface with a vertical resolution of 450 nm. In contrast, the roughness was

measured at a higher resolution over a 10.48 mm² surface area of the sample, at a higher vertical resolution of 102 nm. These measurements can be found below in Table 5-3.

Table 5-3. Surface imaging results.

Surface Imaging Results						
			Top Sample		Bottom Sample	
Sample	Run	TIM	RMS Roughness [μm]	Flatness [μm]	RMS Roughness [μm]	Flatness [μm]
S1	R1	Dry	2.10	531.56	1.42	218.12
S1	R2	Dry	1.91	224.28	1.53	191.63
S1	R3	Dry	2.49	257.73	1.45	456.37
S2	R1	Dry	2.64	393.97	2.25	176.96
S2	R2	Dry	2.22	612.41	1.64	418.11
S2	R3	Dry	2.07	537.97	1.86	163.83
S1	R1	Indium	1.65	200.42	1.33	418.11
S1	R2	Indium	1.86	224.56	1.53	521.11
S1	R3	Indium	2.03	385.63	1.30	208.03
S2	R1	Indium	1.70	425.37	1.75	152.77
S2	R2	Indium	1.77	622.33	1.87	250.03
S2	R3	Indium	1.49	421.49	1.58	149.59
S1	R1	Grease	1.91	485.89	1.24	448.57
S1	R2	Grease	1.28	310.53	1.23	536.56
S1	R3	Grease	1.35	495.83	1.26	179.19
S2	R1	Grease	1.61	546.62	1.65	155.21
S2	R2	Grease	1.38	365.19	1.26	624.59
S2	R3	Grease	1.58	609.56	1.31	273.02

Images of these surfaces are presented in Figure 5-7 below. These images reflect the 5x scan of the total surfaces. In general, the surface roughness was in the range of 1-2 microns and the flatness was in the range of 0.1-0.6 millimeters. The effect of disparities in flatness can be observed within the pressure paper measurements taken showing the contact area and pressure distribution.



Figure 5-7. Alicona G4 InfiniteFocus copper surface imaging.

5.3.2 Pressure Application

The Super Low Fujifilm pressure paper was utilized to collect readings of pressure application before every measurement and scanned. These pressure paper scans can be seen below in Figure 5-8.

Qualitatively, we can see that there is a fairly even distribution of the high-pressure application. In some

instances, such as S1R2 Dry and S1R1 Grease, we can see areas in which pressure is lower though and not evenly applied, due to mismatch of the surfaces. But generally, we can see nominally even and flat contacts are made with distributed pressure application. No contacts have distinct high points or peaks of contact.


S1R1 Dry	S1R2 Dry	S1R3 Dry
		
S2R1 Dry	S2R2 Dry	S2R3 Dry
		
S1R1 Indium	S1R2 Indium	S1R3 Indium
		
S2R1 Indium	S2R2 Indium	S2R3 Indium
		
S1R1 Grease	S1R2 Grease	S1R3 Grease
		
S2R1 Grease	S2R2 Grease	S2R3 Grease
		

Figure 5-8. Pressure paper records for test matrix.

5.3.3 Comparison with Literature

The contacts we characterized performed similarly but slightly better, with lower resistance, in comparison to the past NGC characterization [10]. A graphical comparison of our experimental data and the NGC area-specified data are shown in Figure 5-9 for dry contacts and Figure 5-10 for indium contacts. As can be seen from the plots, the contact resistance data collected in our characterization is slightly lower but follows the same trend and is fairly close in magnitude to the NGC characterization, as expected with the conditions and materials utilized, i.e. the contact pressure magnitude.

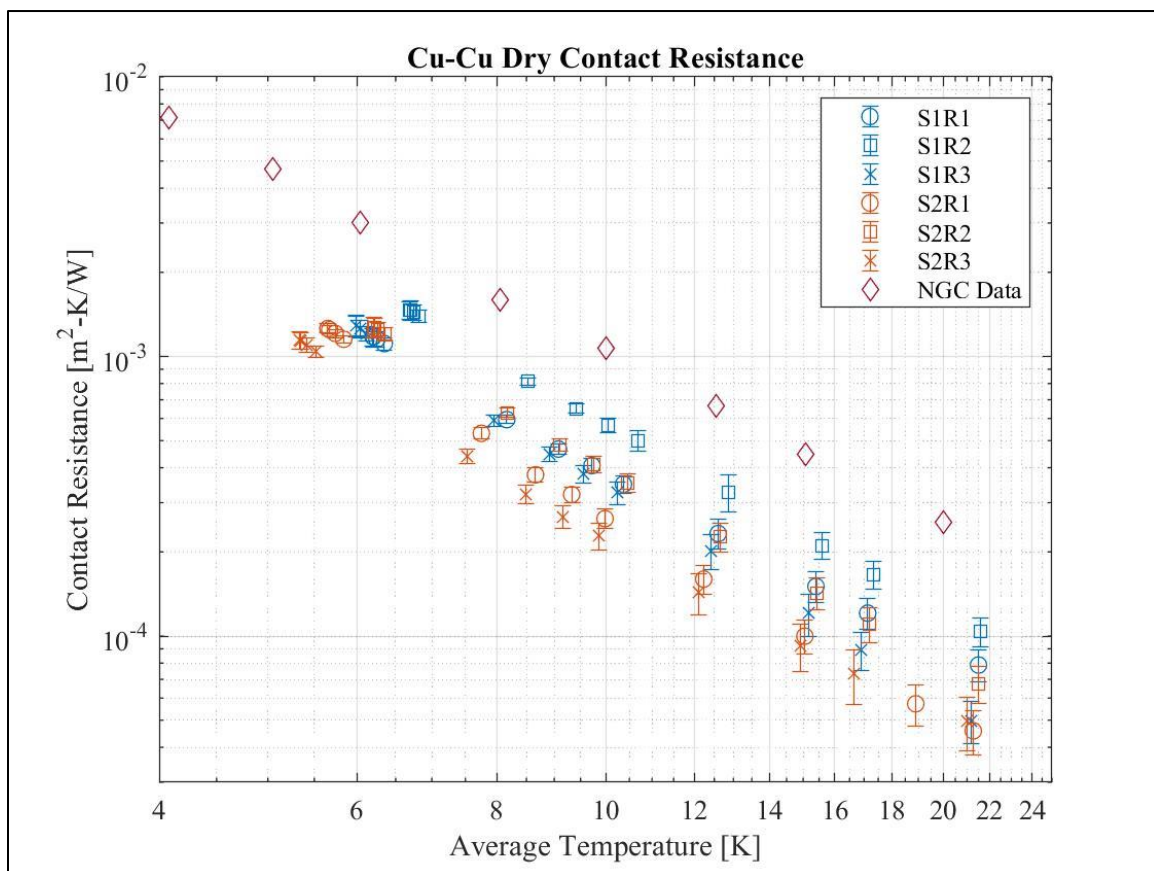


Figure 5-9. Comparison of dry Cu-Cu results with NGC data.

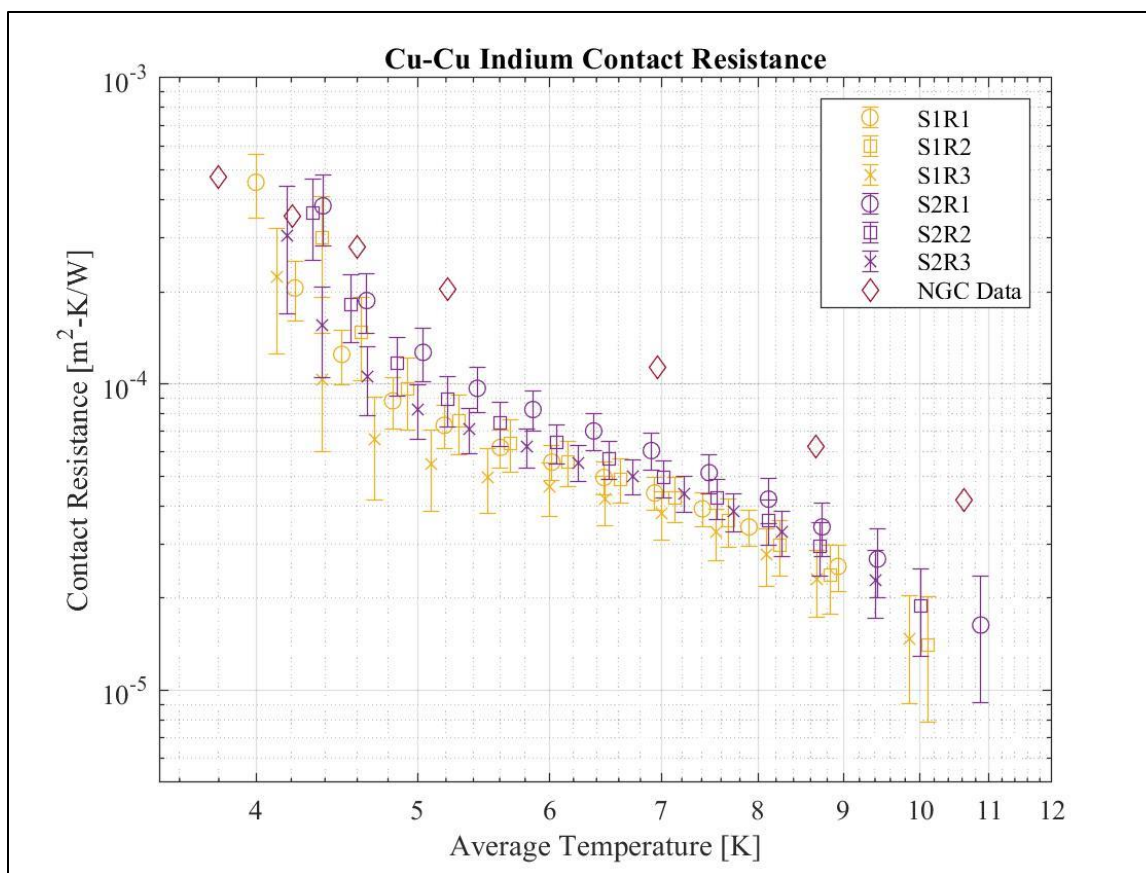


Figure 5-10. Comparison of indium Cu-Cu results with NGC data.

6 Correlations and Theoretical Analysis

6.1 Constriction and Diffuse Mismatch Model

Utilizing the constriction and diffuse mismatch model described in Chapter 2.3, we are able to use our surface roughness data as well as our bulk conductivity data and known applied pressure to estimate the contact resistance of the characterized dry Cu-Cu contacts. The comparison was calculated for several measurements utilizing their specific roughness measurements. These can be seen in Figure 6-1 and Figure 6-2 for S1R1 and S2R1 dry contacts, comparing the results to the theoretical calculated resistance. For these dry Cu-Cu results we find that the model estimates roughly an order of magnitude lower contact resistance than is experimentally observed but follows a similar shaped power law relation as our data. This model and its theoretical calculations yielding much lower estimated contact resistance in comparison to experimental results has been observed with other data found in the literature. Dhuley, in surveying experimental work found that of 25 experimental characterizations, found that only 11 matched within 10-fold of the theoretical resistance given by this model [4].

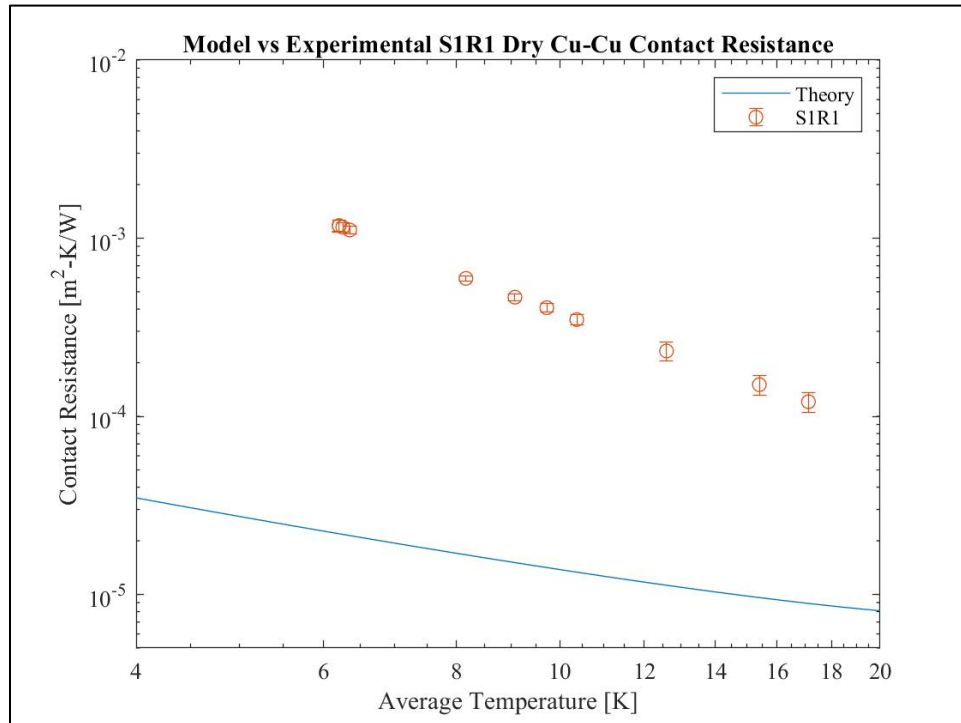


Figure 6-1. Theoretical comparison to S1R1 Dry.

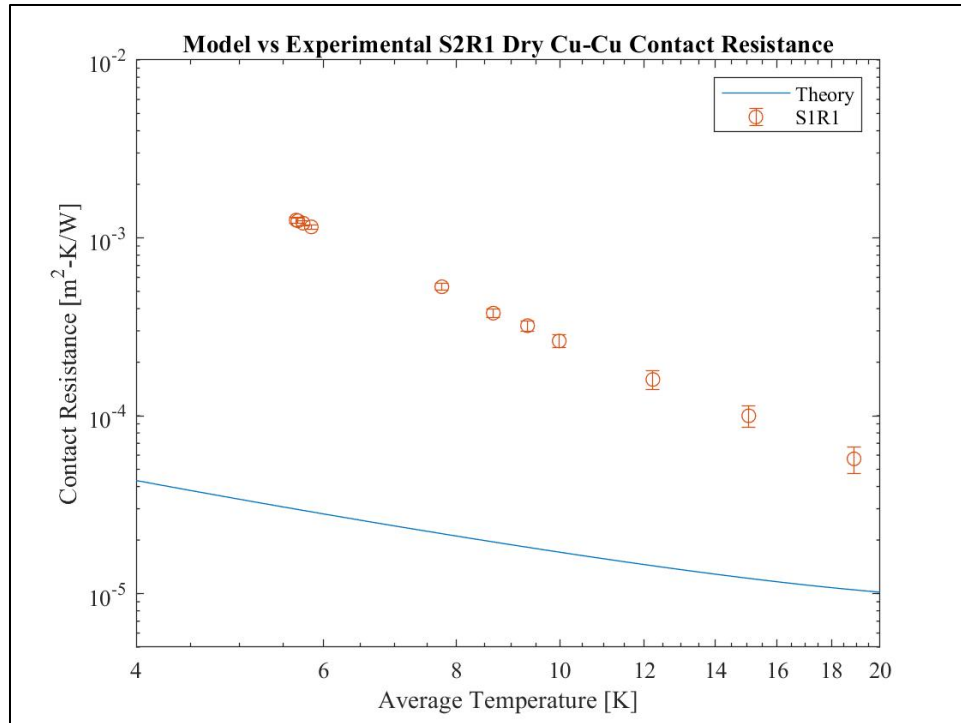


Figure 6-2. Theoretical comparison to S2R1 Dry.

7 Conclusions and Future Work

In this work, a test rig for cryogenic thermal conductivity and thermal contact resistance was successfully designed, fabricated, and validated. Within this experimental setup, an effective liquid helium pot was designed and fabricated in-house in order to limit temperature oscillations on the test platform. The cold plate platform acts as a sample stage and is versatile; it can be utilized for differing test fixtures if required in the future.

In bulk conductivity characterization, it was found that the copper samples generally matched one another's bulk conductivity, with one outlier C110 sample. The conductivities of the two coppers tested, C101 and C110, were observed to be substantially lower than expected for materials of that level purity. The C101 samples were observed to exhibit a bulk conductivity indicative of a RRR value in the range of 70-80.

With all contact resistance measurements, surface measurements and pressure paper readings were performed to enrich the available dataset. Data reduction accounted for fixture resistance and bulk conductivity effects as well as the uncertainty related to all instrumentation. We observed the greatest variation in the dry sample data between samples and mate/de-mate cycles. Each sample's trials for each given condition were given a curve power fit utilized to examine the percent deviation of each sample's runs at an average temperature of 6 K. The lowest deviations were found for the grease samples, which varied a maximum of $\pm(5.9\%, 11.0\%)$ and $\pm(10.3\%, 9.9\%)$ for samples 1 and 2 respectively. The deviation in the indium sample 1 was $\pm(17.7\%, 10.6\%)$ and in sample 2 was $\pm(14.7\%, 16.8\%)$. As mentioned, the highest deviations were observed for the dry contacts, equaling $\pm(15.5\%, 27.9\%)$ for sample 1 and $\pm(24.2\%, 27.0\%)$ for sample 2.

The collected data was verified against past NGC data to be close in magnitude for the similar conditions. The theoretical constriction and diffuse mismatch model varied largely from the dataset though, predicting much lower resistances than observed.

Future work with this experimental test rig will expand into further characterizations and testing of novel solutions to improve contact resistance. There are many materials and cryogenic packaging needs that can be better understood with thorough thermal characterization.

References

- [1] M. Kanellos, "Moore's Law to roll on another decade," CNET, 11 February 2003. [Online].
Available: <https://www.cnet.com/news/moores-law-to-roll-on-for-another-decade/>.
- [2] W. Buckel and R. Kleiner, "Fundamental Properties of Superconductors," in *Superconductivity, Fundamentals and Applications*, Wiley, 2008, pp. 11-69.
- [3] B. Averill and P. Eldredge, "12.7 Superconductors," in *General Chemistry: Principles, Patterns, and Applications*, Saylor Foundation, 2011.
- [4] R. Dhuley, "Pressed copper and gold-plated copper contacts at low temperatures - A review of thermal contact resistance," *Cryogenics*, vol. 101, pp. 111-124, 2019.
- [5] C. V. Madhusudana, Thermal Contact Conductance, New York, NY: Springer-Verlag New York Inc., 1996.
- [6] J. Tuttle, E. Canavan and A. Jahromi, "Cryogenic thermal conductivity measurements on candidate materials for space missions," *Cryogenics*, vol. 88, pp. 36-43, 2017.
- [7] C. A. Thompson, W. M. Manganaro and F. R. Fickett, "Cryogenic Properties of Copper," Copper Development Association Inc., July 1990. [Online]. Available:
<https://www.copper.org/resources/properties/cryogenic/>.
- [8] S. W. Van Sciver, M. J. Nilles and J. Pfotenhauer, "Thermal and Electrical Contact Conductance Between Metals at Low Temperatures," *Proceedings of 1984 Space Cryogenics Workshop*, pp. 37-48, 1984.
- [9] E. Gmelin, M. Asen-Palmer, M. Reuther and R. Villar, "Thermal boundary resistance of mechanical contacts between solids at sub-ambient temperatures," *Journal of Physics D: Applied Physics*, vol.

32, 1999.

- [10] A. Dillon, K. McCusker, J. Van Dyke, B. Isler and M. Christiansen, "Thermal interface material characterization for cryogenic electronic packaging solutions," *IOP Conf. Series: Materials Science and Engineering*, vol. 278, 2017.
- [11] L. J. Salerno and P. Kittel, "Technical Memorandum 110429: Thermal Contact Conductance," NASA, 1997.
- [12] L. J. Salerno, P. Kittel and A. L. Spivak, "Technical Memorandum 858621: Thermal Conductance Measurements of Pressed OFHC Copper Contacts at Liquid Helium Temperatures," NASA, 1983.
- [13] M. M. Yovanovich, "Thermal contact correlations," *American Institute of Aeronautics and Astronautics, Thermophysics Conference, 16th*, pp. 81-1164, 1981.
- [14] B. C. Gundrum, D. G. Cahill and R. S. Averback, "Thermal conductance of metal-metal interfaces," *Physical Review B - Condensed Matter and Materials Physics*, vol. 72, no. 24, pp. 1-5, 2005.
- [15] NIST, "Material Properties: OFHC Copper (UNS C10100/C10200)," 3 February 2010. [Online]. Available: https://trc.nist.gov/cryogenics/materials/OFHC%20Copper/OFHC_Copper_rev1.htm.
- [16] NIST, "Material Properties: 6061-T6 Aluminum (UNS A96061)," [Online]. Available: https://trc.nist.gov/cryogenics/materials/6061%20Aluminum/6061_T6Aluminum_rev.htm.
- [17] Tekscan, "Fujifilm Prescale Film," [Online]. Available: <https://www.tekscan.com/products-solutions/pressure-sensing-film/fujifilm-prescale-film>.
- [18] Lake Shore Cryotronics, Inc., "Lake Shore Model 218 Temperature Monitor User's Manual," 25 July 2017. [Online]. Available: <https://www.lakeshore.com/docs/default-source/product->

downloads/218_manual.pdf?sfvrsn=1ea170a7_1.

[19] Sequoia Brass & Copper, "Copper," [Online]. Available: <https://www.sequoia-brass-copper.com/copper/>.

[20] Thermal Space and Thermal Straps, "Thin Metal Foil Thermal Straps (TMF Series)," 2016. [Online]. Available: <https://thermal-space.com/thermal-straps/thin-metal-foil-thermal-straps/>.

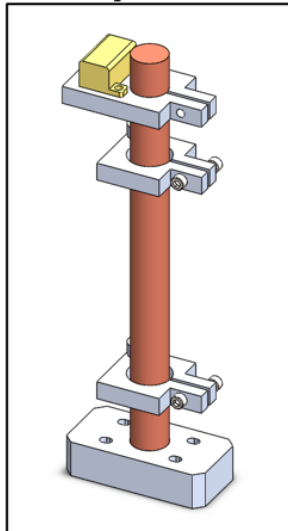
[21] J. Tuttle, E. Canavan and M. DiPirro, "Thermal and Electrical Conductivity Measurements of CDA 510 Phosphor Bronze," *AIP Conference Proceedings*, vol. 1219, no. 1, pp. 55-62, 2010.

Appendix A. Bulk Conductivity Test Procedure and Data Processing

1 Test Procedure

1.1 Sample Preparation

Samples for the bulk conductivity testing consist of 6-inch long, $\frac{1}{2}$ -inch diameter copper rods. Mounting these samples is described below.



1. Mount the knife-edge sensors with attached temperature sensors onto the rod. T1 is mounted at the top of the rod and T2 is mounted below it. The bottom of the rod is distinguished by a threaded hole for mounting to the aluminum base.
2. Record five measurements each of the diameter of the rod and the length between the knife-edges of the two temperature sensor clamps. For example:

	1	2	3	4	5	Avg
Diameter (m)						
Length (m)						

3. Mount the heater clamp to the top of the rod. Ensure the heater leads are connected to the power supply and the multimeter, two sets of two wire leads. This can be verified by testing the heater function and measurement of power in the LabView test code. If the code reads a negative power output one of the two sets of leads simply needs to be reversed for the correct 4-wire measurement.
4. Mount the copper rod into the aluminum sample base with a #4-40 bolt ensuring a tight secure mounting. Indium foil should be placed in the contact between the rod and the aluminum base.
5. Then, mount the aluminum base onto the sample stage with four #4-40 bolts. Again, ensure indium is in place between the contact of the sample stage and the aluminum base.

1.2 Sensor Check

Once the sample is successfully mounted onto the copper sample stage, ensure the temperature sensors and heaters (trim and main) are all functioning and recording data correctly with the LabView main code.

1. Ensure all instrumentation is on, specifically the BK Precision 1687B, BK Precision 1698, HP 34401A, Keithley 2000, and Lakeshore 218. Temperature sensors T1 and T2 at room temperature should read out a resistance on the Lakeshore screen of ~ 70 ohms, and T3, T4, T5 and T6 should read a resistance of ~ 3 -4 ohms.
2. Ensure heaters are both connected. H1 is the main heater and requires a four-wire connection. One two-wire set connects to the power supply BK 1698 and the other connects to the Keithley

1. 2000 multimeter for voltage reading. H2 is the trim heater, and the two-wire lead connects it to the BK 1687B power supply.
2. Run the TEST_MAIN LabView code to ensure heaters are running properly.
 - a. Set trim heater to 5V output to ensure it reads a power output then set back to zero.
 - b. Set main heater to 1V output to ensure it reads correct output and then set back to zero.

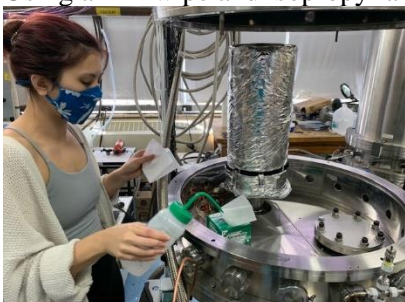
1.1 System Closing and Preparation

After mounting the sample and checking sensors, begin closing the thermal jackets and vacuum chamber can begin to close the system to begin testing. A few warnings for handling within this portion, **do not place tools on the vacuum chamber edge and always wear gloves when handling MLI.**

1. Beginning with the second stage inner jacket, carefully place the jacket over the sample stage and tightly bolt the jacket in place (6 bolts).
2. Velcro the MLI of the inner jacket together (4 straps).



3. Place the bottom flange and outer jacket (the larger MLI covered aluminum can) carefully onto the first stage. **ENSURE no wires or pinched or disconnected in this process and perform a second sensor check after placing the jacket down.** Tightly bolt the jacket and flange into place (8 bolts) and attach the extra strips of MLI around the flange.
4. Attach the bottom MLI to the MLI around the outer jacket with the 4 Velcro strips. **Ensure no MLI sheets from the jacket are touching the vacuum chamber walls.**
5. Using a Kimwipe and isopropyl alcohol, clean the inside and edge of the vacuum chamber.



6. **BEFORE CLOSING THE VACUUM CHAMBER, ensure nothing such as tools are left within the chamber.**
7. Lower the bell jar of the vacuum chamber slowly with one hand supporting it as it lowers, ensuring not to touch the chamber O-ring.

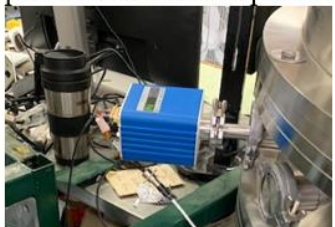


8. Fasten the six bolts on the vacuum chamber in a star pattern and then in a circle, like bolting a tire, to ensure an even bolting.



1.4 Starting Vacuum

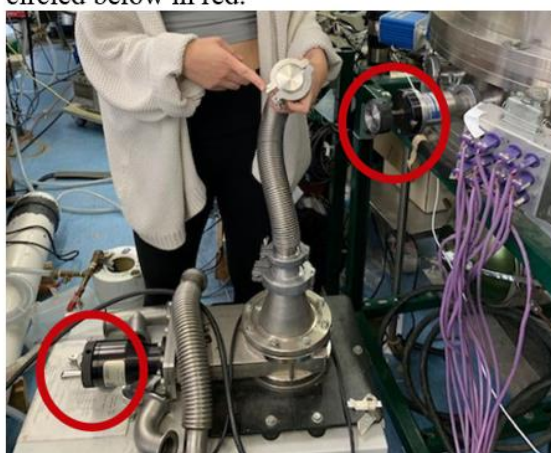
1. Ensure the vacuum gage (Granville Phillips Micro-Ion Plus) is turned on and powered. It is powered with a wall power adaptor.



2. Secure the vacuum hose attached to the vacuum cart to the chamber valve. This is a KF-flange fitting, which is connected with an O-ring between the hose and the fitting on the chamber. Tighten the clamp around the connected fittings by hand.



3. Ensure that the pump valve and chamber valve are both opened. These two valve knobs are circled below in red.



4. With the vacuum pump plugged in to its wall power supply, flip the switch labeled 'convertor' to the on position to turn on the electronics of the vacuum pump.
5. Then, flip on the 'vane pump' switch to turn on the roughing pump.
6. Monitoring the chamber pressure with the LabView code 'vacuum gauge readout', wait until the chamber pressure is below 0.1 Torr before turning on the turbo pump.
7. Before turning on the turbo pump, check the vacuum chamber bolts and tighten if needed.
8. Press the 'start' button on the vacuum cart below the convertor and vane pump switches to turn on the turbo pump.
9. After the turbo pump is on and the chamber pressure is below 0.02 Torr, the cryocooler can be turned on.

1.5 Starting the Cryocooler

1. Turn on the power supply to the pump running the water cooling the compressor. The pump runs at max 10 V for power input, usually run for our purposes at 9-10V.



2. Check the water in the reservoir is sufficient. The reservoir is the tubing above the T-joint into the closed loop pump seen in the photo above. There should be water above the T-joint while running. If it is low, add distilled water.
3. Turn on the facility water to the heat exchanger by opening the red valve. It is shown here in the open position. If turned parallel to the ground, it is in the closed position.



4. Turn the main power switch of the compressor to 'on'. This is vertical as shown in the picture circled in red.



5. Press the 'On' button on the compressor to start running. This is shown in the picture below circled in red.



1.6 Data Collection

An example of the data collection test matrix is given for C101 S1 in the example data section.

1. Once the experiment has reached cold steady state, testing can begin. To begin recording data, press the 'recording' button on the LabView 'TEST_MAIN' code. **Ensure the file path string includes the file name you would like to store this file under.**
2. First, parasitic testing is completed to account for parasitic temperature differentials. The trim heater is adjusted in set increments while the main heater is kept at zero power. After each setpoint is set, it is allowed to reach steady state to record a temperature dependent relation of this parasitic.
3. Once the parasitic relation has been recorded the main data can be tested. A set of nominal goal average temperatures between the two recorded temperatures are tested. These were achieved with a combination of usage of the trim and main heaters. These combinations were chosen based on maintaining a minimum dT for a given uncertainty, shown in the test protocol below. Adjusting the main heater adjusts the dT in addition to the average temperature, while the trim heater affects only the average temperature and not the dT.

1.6.1 Test Protocol

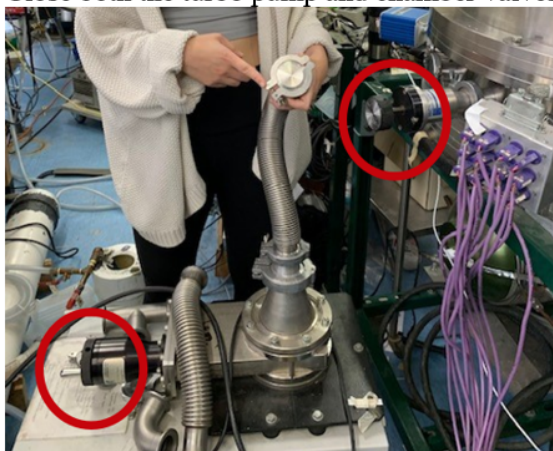
Bulk Conductivity Test Nominal Temperature Setting Matrix					
dk/k = 5%		dk/k = 10%		dk/k = 15%	
Average T	Minimum dT	Average T	Minimum dT	Average T	Minimum dT
4.5	0.1814	4.5	0.08871	4.5	0.05888
5	0.1929	5	0.09435	5	0.06263
5.5	0.2066	5.5	0.101	5.5	0.06707
6	0.2222	6	0.1087	6	0.07214
6.5	0.2395	6.5	0.1172	6.5	0.07779
7	0.2585	7	0.1265	7	0.08396
8	0.3006	8	0.1471	8	0.09769
9	0.3478	9	0.1702	9	0.113
10	0.3994	10	0.1955	10	0.1298
12	0.514	12	0.2517	12	0.1671
15	0.712	15	0.3487	15	0.2316
20	1.105	20	0.5412	20	0.3594
30	2.117	30	1.037	30	0.6883
40	3.428	40	1.676	40	1.113

1.7 Cryocooler Off and Returning to Room Temperature

1. Press the 'off' button on the compressor to the left of the 'on' button.
2. Turn the main power switch on the compressor to the off position.
3. Turn the facility water red valve to the closed position.
4. Turn off the water pump power supply.
5. Set the main heater to 25 V and the trim heater to 37 V to heat the experiment to room temperature, which generally takes half a day to equilibrate.

1.8 Stopping Vacuum and Opening the Chamber

1. Remove all the bolts on the vacuum chamber.
2. Close both the turbo pump and chamber valves.



3. Undo the clamp connected the hose of the vacuum cart to the chamber valve to separate the vacuum cart and the chamber.
4. Stop the turbo pump by pushing the 'stop' button.
5. Stop the roughing pump by switching the vane pump to off.
6. Turn off the electronics by switching the convertor switch to off.
7. **Slowly vent the turbo pump until you hear the spinning change (get slightly louder), then stop adjusting the valve and wait for the turbo to spin down and the sound to stop.**
8. **Once the spinning stops, open the valve all the way to fully expose the turbo pump to room pressure.**
9. Open the vacuum chamber valve slowly to vent the chamber to room pressure as well.
10. Slowly lift the vacuum chamber bell jar open to access the chamber inside.
11. **Put gloves on and take apart the MLI and thermal jackets to access the sample within.**
12. Once the jackets are off, disassemble the sample fixture to prepare for the next test.

2 Data Processing and Calculation

The data from LabView is stored in a TDMS file under the file name given in the input of the code (top left of the screen). Opening this TDMS file, data can be pulled out for each steady-state collection time. The steady-state data is collected in 200 data point entries and copied into the appropriate excel files.

2.1 Parasitic Data

In the parasitic excel file, the data from each setpoint is uploaded to a separate sheet. These sheets are titled 'No load behavior' and '1' through '6'. In the sheet labeled 'Parasitic dT', these data are averaged and plotted with a curve fit power law. Record this curve fit power law, with variables A and B, to be used in processing the main data.

$$dT_{parasitic} = A * T^B$$

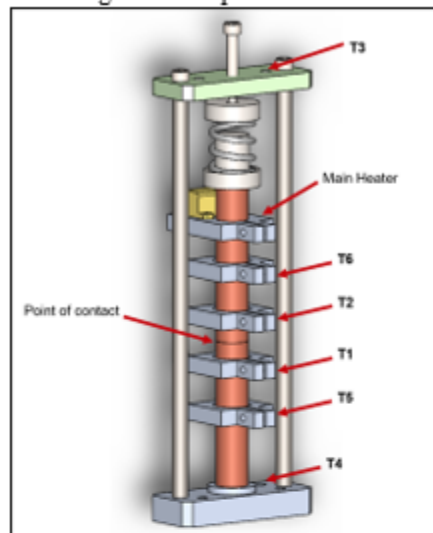
C101 Sample 1 Bulk Conductivity Data					
Avg T [K]	k [W/m-K]	U_T [K]	U_k [W/m-K]	dT [K]	Q [W]
4.47	533.56	0.05	15.74	0.11	0.03
7.20	950.62	0.14	36.78	0.28	0.43
5.17	682.91	0.08	27.80	0.15	0.11
6.09	814.40	0.10	32.96	0.21	0.24
8.38	1094.61	0.17	42.19	0.35	0.67
9.14	1179.48	0.19	47.95	0.38	0.80
9.92	1266.07	0.20	53.68	0.41	0.95
15.29	1765.64	0.37	82.64	0.73	2.53
22.47	2071.16	0.66	99.50	1.32	5.54
30.63	1959.60	1.20	87.31	2.40	9.57
41.42	1519.02	2.36	57.78	4.71	14.67

Appendix B. Contact Resistance Test Procedure and Data Processing

1 Test Procedure

1.1 Sample Preparation

Samples for the contact resistance testing consist of two 2.25-inch long, ½-inch diameter copper rods. Mounting these samples is described below.



1. Mount the knife-edge sensors with attached temperature sensors onto the rod. These sensors are mounted in the order shown above. Ensure the sensors are put on from the far edge (not over the contact be measured) so the contact is not accidentally scratched or hurt. Note that T3 and T4 can be always left in place, and only the clamps with T1, T2, T5 and T6 need to be mounted and remounted to the rods.
2. Record five measurements each of the diameter of the rod and the length between the knife-edges of the temperature sensor clamps and the T1 and T2 sensors' distance from the contact. For example:

	1	2	3	4	5	Avg
Diameter (m)						
Length (m)						
T5-T1 (m)						
T1-Contact (m)						
T2-Contact (m)						
T2-T6 (m)						

3. Mount the heater clamp to the top of the upper rod, ensuring space is left near the top of the rod for the spring holder. Ensure the heater leads are connected to the power supply and the multimeter, two sets of two wire leads.
4. Clean both contact surfaces with isopropyl alcohol and Kim wipes.
5. Record a pressure paper measure by placing pressure paper between the contact and placing the spring assembly on top. Screw the spring assembly tight to the desired pressure with the #8-32 bolt on top.
6. Remove the pressure paper and reclean the surfaces. If a TIM is to be used, apply now.
7. Re-mount the contact with the spring assembly in place and secure to desired pressure with the #8-32 bolt on top.
8. Then, mount the aluminum base onto the sample stage with four #4-40 bolts. Again, ensure indium is in place between the contact of the sample stage and the aluminum base.

1.2 Sensor Check

*Follow Bulk Conductivity Test Procedure [1.21.7 Sensor Check](#) procedure.

1.3 System Closing and Preparation

*Follow Bulk Conductivity Test Procedure [1.31.7 System Closing and Preparation](#) procedure.

1.4 Starting Vacuum

*Follow Bulk Conductivity Test Procedure [1.4 Starting Vacuum](#)1.7Starting the Cryocooler procedure.

1.5 Starting the Cryocooler

*Follow Bulk Conductivity Test Procedure [1.5 1.7Starting the Cryocooler](#) procedure.

1.6 Data Collection

An example of the data collection test matrices for dry, grease and indium measurements are given in the example data section.

1. Once the experiment has reached cold steady state, testing can begin. To begin recording data, press the 'recording' button on the LabView 'TEST_MAIN' code. **Ensure the file path string includes the file name you would like to store this file under.**
2. First, parasitic testing is completed to account for parasitic temperature differentials. The trim heater is adjusted in set increments while the main heater is kept at zero power. After each setpoint is set, it is allowed to reach steady state to record a temperature dependent relation of this parasitic.
3. Once the parasitic relation has been recorded the main data can be tested following the test matrices for a given type of contact. For dry contacts, low main heater input can be kept while adjusting the trim and readings can be found up to 20 K. For dry and grease measurements, due to their very low resistance and dTs, the main heater must be mainly used without the trim, and readings can be measured with reasonable uncertainty up to 10 K. Adjusting the main heater adjusts the dT in addition to the average temperature, while the trim heater affects only the average temperature and not the dT.

1.7 Cryocooler Off and Returning to Room Temperature

*Follow Bulk Conductivity Test Procedure [1.7 1.7Cryocooler Off and Returning to Room Temperature](#) procedure.

1.8 Stopping Vacuum and Opening the Chamber

*Follow Bulk Conductivity Test Procedure [1.8 Stopping Vacuum and Opening the Chamber](#) procedure.

2 Data Processing and Calculation

The data from LabView is stored in a TDMS file under the file name given in the input of the code (top left of the screen). Opening this TDMS file, data can be pulled out for each steady-state collection time. The steady-state data is collected in 200 data point entries and copied into the appropriate excel files.

2.1 Filing Format

To utilize the MATLAB code, the script 'rundatamainuncertainty.m' is run. This processes all the data pulled from three excel files within a folder titled after the run. For example, to run the data for a run titled 'S1R1 DRY' the runnumberset variable in this script, line __, equal to this string. The folder will then be labeled S1R1 DRY and the files within will all be labeled accordingly 'S1R1 DRY Measurements', 'S1R1 DRY_mainparasitic', and 'S1R1 DRY_maindata' to be correctly called within the

MATLAB script. Once the script is run, a figure is plotted, and the calculated data is stored in a 'MainData.xls' excel file under a sheet titled the runnumberset variable. In the example case, 'S1R1 DRY'.

2.2 Physical Measurements

The measurements taken in section 1.1 must be recorded in a excel file labeled in the format 'runnumberset Measurements.xlsx'. An example can be found in the file 'S1R1 DRY Measurements'. The format for the storage of data is:

	A	B	C	D	E	F
1	Top Diameter (m)	Bottom Diameter (m)	T6-T2 (m)	T2-Contact (m)	Contact-T1 (m)	T1-T5 (m)
2	0.01266	0.01265	0.00787	0.01202	0.01636	0.01195
3	0.01269	0.01268	0.00806	0.01212	0.01656	0.01236
4	0.01267	0.01267	0.00845	0.01206	0.01645	0.01205
5	0.01268	0.01266	0.00807	0.01215	0.01617	0.01222
6	0.01265	0.01268	0.00807	0.01219	0.01646	0.01188

2.3 Parasitic Data

In the parasitic excel file, the data from each setpoint is uploaded to a separate sheet. These sheets are titled '1' through '8'. The power fit law is calculated and accounted for by the MATLAB script. The example file 'S1R1 DRY_mainparasitic' is available.

2.4 Main Data

In the main data excel file, the 200-data point collections for the twelve measured set points are pulled from the TDMS file into the sheets labeled '1' through '12' accordingly. Data is then processed in the MATLAB script after this file, the parasitic file, and the measurement file are all completed and placed in the appropriately run number labeled folder.

2.5 Example Data – S1R1 DRY

The S1R1 DRY runs' test matrix, collected data, associated excel sheets of processed data, and physical sample are available as an example and for training. Please note that the data was collected with a working T1 Cernox sensor that has since broken so considerations for formula calculations and uncertainty would need to be changed if the data is recollected with a different sensor. Note that the trim heater utilized is a 30-ohm cartridge heater with a maximum power input of 50 W.

Test Matrix for Sample 1 Run 1 DRY		
Data	Trim Heater Set Voltage [V]	Main Heater Set Voltage [V]
Parasitic	0	0
	4	0
	8	0
	12	0
	16	0
	20	0
	24	0
	28	0
Main	0	2
	1	2
	2	2
	3	2
	11	2
	14	2

	16	2
	18	2
	22	2
	24	2
	25	2
	27	2

Sample 1 Run 1 DRY Resistance Data			
Average Temperature [K]	Resistance [m^2K/W]	$dT/2$ [K]	U_R [m^2K/W]
6.21	0.001175	1.14	9.41E-05
6.20	0.001178	1.15	8.48E-05
6.25	0.001153	1.13	7.22E-05
6.35	0.001112	1.10	5.77E-05
8.16	0.000594	0.68	2.03E-05
10.38	0.000349	0.45	2.47E-05
9.08	0.000466	0.56	2.05E-05
9.72	0.000407	0.50	2.3E-05
12.60	0.000233	0.32	2.84E-05
15.40	0.000151	0.23	1.9E-05
17.13	0.000121	0.20	1.51E-05
21.50	7.88E-05	0.15	1.05E-05

*ALSO NOTE that for grease and indium data, due to the very low resistance and small dTs observed, varied testing matrices had to be utilized where all heat was input through the main heater to maximize dTs. Two examples are shown.

Example Test Matrix for GREASE Contact Measurements		
Data	Trim Heater Set Voltage [V]	Main Heater Set Voltage [V]
Parasitic	0	0
	4	0
	8	0
	12	0
	16	0
	20	0
	24	0
	28	0
Main	0	2
	0	2.5
	0	3
	0	3.5
	0	4
	0	4.5
	0	5
	0	5.5
	0	6
	0	7
	0	8
	0	9

Example Test Matrix for INDIUM Contact Measurements		
Data	Trim Heater Set Voltage [V]	Main Heater Set Voltage [V]
Parasitic	0	0
	4	0
	8	0
	12	0
	16	0
	20	0
	24	0
	28	0
Main	0	1
	0	1.5
	0	2
	0	2.5
	0	3
	0	3.5
	0	4
	0	4.5
	0	5
	0	5.5
	0	6
	0	7